Report 2955

NAVAL SHIP RESEARCH AND DEVELOPMENT CENTER
Washington, D.C. 20007

NUMERICAL SOLUTION OF THE INCOMPRESSIBLE TIME-DEPENDENT VISCOUS FLOW PAST A THIN OBLATE SPHEROID

APPLIED MATHEMATICS LABORATORY
RESEARCH AND DEVELOPMENT REPORT

January 1969

Report 2955

NUMERICAL SOLUTION OF THE INCOMPRESSIBLE TIME-DEPENDENT VISCOUS FLOW PAST A THIN OBLATE SPHEROID

The Naval Ship Research and Development Center is a U.S. Navy center for laboratory effort directed at achieving improved sea and air vehicles. It was formed in March 1967 by merging the David Taylor Model Basin at Carderock, Maryland and the Marine Engineering Laboratory at Annapolis, Maryland. The Mine Defense Laboratory, Panama City, Florida became part of the Center in November 1967.

Naval Ship Research and Development Center
Washington, D.C. 20007

NDW-NSRDC 3960/43 (10-67)

DEPARTMENT OF THE NAVY
NAVAL SHIP RESEARCH AND DEVELOPMENT CENTER
WASHINGTON, D. C. 20007

NUMERICAL SOLUTION OF THE INCOMPRESSIBLE TIME-DEPENDENT VISCOUS FLOW PAST A THIN OBLATE SPHEROID

by

Yermiyahu Rimon

January 1969 Report 2955

TABLE OF CONTENTS

LIST OF FIGURES

NOTATION

a	Focal distance; the distance between the focus of the obstacle and the centerline.
b, d, e	Coefficients in the line relaxation.
C_D, C_{DF}, C_{DP}	Total, friction, and pressure drag coefficients.
C_V	Contour value of a plotted line.
c	The nondimensional metric coefficient of the η and θ coordinates
D, D_F, D_P	Total, friction and pressure drag.
$EDER$	Terms which are off the line of relaxation.
$EPSIL$	Accuracy governing factor in the iterative process.
G, ST	Terms in the recursion formula of the line relaxation.
h	Length increment of the grid.
NTS	Number of time steps.
P	Pressure.
Q	Source term in the line relaxation.
$\mathrm{R_e} = \frac{2Ua}{\nu}$	Reynolds number based on focal diameter.
RF	Overrelaxation parameter.
r, ϕ, z	The cylindrical polar coordinates.
t	Time.
U	Uniform flow velocity at infinity.
$\vec{u}$	Velocity vector.
u	Velocity component in the axial direction.
v	Velocity component in the radial direction.
α	Angle between the normal to the body and the z-axis.
δt	Time step.

η, θ, ϕ	Oblate-spheroidal coordinates.
μ	Viscosity.
$\nu = \frac{\mu}{\rho}$	Kinematic viscosity.
ρ	Density.
τ	Friction stress.
ψ	Stream function.
$\vec{\omega} = \nabla \times \vec{u}$	Vorticity vector.
ω	Vorticity component in the azimuthal direction.
∇	Del operator.

Subscripts

0	Of the stagnation point.
b	Of the body.
f	Of the outer boundary.
i, j	Counters of the grid points in the η and θ direction.
IL, JL	The ranges of the i and j subscripts.
L	Of the last time step.
max	Maximum.
min	Minimum.
s	Of the separation point.
η	Of the η direction.
θ	Of the θ direction.

Superscripts

k	Counter of iterations.
n	Counter of time steps.
$'$	Physical dimensional quantities.

ABSTRACT

The objective of this work is to obtain numerical solutions of the transient flow around a thin disk normal to the flow. The transition takes place between a potential field and a fully developed viscous field. The fluid is incompressible and homogeneous, and its flow is governed by the Navier-Stokes equations.

The purpose of the study is twofold: (1) to investigate the effects of a very large curvature of the body on the numerical procedure for the solution of the flow field and (2) to investigate the fundamental fluid dynamical phenomena of separation, of a recirculatory wake, and of vorticity shedding under the constraint of axial symmetry.

The solutions are obtained by constructing a finite-difference approximation to the Navier-Stokes equations on an oblate spheroidal grid system, and then advancing the solution with respect to time. The vorticity and the stream function are the dependent variables.

The results show that no vorticity shedding occurs for axisymmetric flow in the Reynolds-number range studied. In addition, some new interesting fluid-dynamical features are revealed. These include a different behavior of the pressure distribution at low and high Reynolds numbers and a local maximum of vorticity inside the wake at the higher Reynolds numbers studied.

ADMINISTRATIVE INFORMATION

This study was supported by the Naval Ship Systems Command under the Mathematical Sciences Program. Funding was under Subproject S-R003 10 01, Task 11572. The date of completion was 1 July 1968.

INTRODUCTION

This report deals with the numerical solution of the unsteady flow field past a thin oblate spheroid. The obstacle is impulsively set into a uniform motion. The fluid is assumed to be homogeneous, incompressible, and governed by the Navier-Stokes equations including viscous terms.

The flow past a thin disk has long attracted the interest of fluid dynamicists. The complicated phenomena of the recirculatory wake behind the disk and the eventual shedding of vorticity in the form of "horseshoe" rings as the Reynolds number increases have been

dealt with in many experimental investigations.[1-3] The even more intriguing question of the nature of the flow field around an infinitely thin disk, especially at the singular point at the edge of the disk, has recently evoked controversy.[4, 5]

The nonlinear terms of the governing equations are of a magnitude that cannot be neglected or estimated over the Reynolds number range of interest. Thus, a closed-form solution of the system of differential equations is beyond the state of the art at the present time. As a result, we were led to seek a numerical solution to the problem that might shed some light on the fluid dynamical processes that take place. At the same time, the method developed provides a tool for the solution of other problems heretofore unsolvable.

The art of obtaining numerical solutions to fluid dynamical problems (for even today this involves a great deal of art in addition to science) lay dormant since its inception in the twenties by Thom[6] until the late fifties. Some very interesting relaxation techniques were developed during that period, but the large volume of computation associated with their application has limited their practicality. The renaissance of these methods in recent years is linked with the tremendous advance in high-speed computers. Several investigations[7-10] have demonstrated the feasibility of obtaining qualitative and quantitative solutions to extremely complicated problems related to viscous flow phenomena.

In a previous work,[10] the author obtained a quantitative solution to the flow past a sphere. Preparatory work for the sphere solution gave a crude solution of flow over a disk with sharp corners. Even that crude work indicated the extreme importance of the correct handling of sharp corners in representing the development of the recirculatory wake. In that work, closed loops of equal vorticity lines were formed at the end of the wake and were convected and diffused downstream (Figure 14 of Reference 10). No such loops were observed in the much more careful and accurate sphere solution despite the fact that "horseshoe" rings of separated vorticity have been observed experimentally for the sphere.[11]

Both the accurate sphere and the crude disk solutions were strictly axisymmetric whereas the observed vorticity shedding is clearly three-dimensional in nature. Thus, several questions are raised: Is vorticity shedding possible at all in a strict axisymmetric solution? Are the separated loops in the crude disk solution a result of the inaccurate handling of the sharp corners (they were treated according to a suggestion by Fromm[7] as inner points to the fluid) or are they a real axisymmetric equivalence to the observed three-dimensional shedding? The answers to these questions have great bearing on the problem of physical stability of the flow field in the absence of three-dimensional disturbances.

With the above background, it was natural to attempt a careful and accurate solution to a flow past a thin disk. Such a study could also shed light on the controversial problem of the nature of the solution near the edge of the disk. In addition it is a severe test of the numerical techniques used in obtaining the solution. The severity of the numerical test stems

---

[1]References are listed on page 44.

from the large gradients which exist in the field because of the extreme curvature near the edge. These large gradients require a very fine mesh locally and have grave effects on the numerical stability.

In a previous numerical study, Michael[12] solved the case of an infinitely thin disk by the steady-state equations for low Reynolds numbers. His solution was not obtained by a correct treatment of the sharp edge; furthermore, it was a steady-state solution and was not carried to high enough Reynolds numbers. Therefore, his method is not appropriate for the purpose of the present study. Our solution is time-dependent, uses a natural coordinate system for the disk, and is carried beyond the Reynolds number for which vorticity separation has been observed (approximately 170).

To summarize, the purpose of this study is twofold: (1) to investigate the effect of a very large curvature of the body on the flow both numerically and physically and (2) to investigate the fundamental fluid dynamical phenomena of separation, of a recirculatory wake, and of vorticity shedding under the constraint of axial symmetry. Additional information and discussion of the nature of the flow field near a sharp edge will be presented in a subsequent report.

FORMULATION

GOVERNING EQUATIONS

The vector form of the Navier-Stokes equations for an incompressible, homogeneous fluid (ρ = const) with constant viscosity μ and no body forces is:

$$\left(\frac{\partial}{\partial t} + \vec{u} \cdot \nabla\right) \vec{u} = -\frac{1}{\rho} \nabla P + \nu \nabla^2 \vec{u} \qquad [1]$$

Using the relation $(\vec{u} \cdot \nabla)\, \vec{u} = \nabla\, (1/2\ \vec{u}^{\,2}) + \vec{\omega} \times \vec{u}$, where $\vec{\omega} = \nabla \times \vec{u}$ is the vorticity, we obtain:

$$\frac{\partial \vec{u}}{\partial t} + \vec{\omega} \times \vec{u} = -\nabla \left(\frac{P}{\rho} + \frac{1}{2} \vec{u}^{\,2}\right) + \nu \nabla^2 \vec{u} \qquad [2]$$

By taking the curl of Equation [2], we arrive at the vorticity transport equation in vector form

$$\frac{\partial \vec{\omega}}{\partial t} + \nabla \times (\vec{\omega} \times \vec{u}) = \nu \nabla^2 \vec{\omega} \qquad [3]$$

The continuity equation for an incompressible homogeneous fluid is:

$$\nabla \cdot \vec{u} = 0 \qquad [4]$$

We will restrict the study to axial symmetry by not allowing any variations with the azimuthal angle. The reason for this restriction is the inability of present computers to handle three-dimensional problems accurately because of limitations in their speed and storage capacity. Even the present axisymmetrical calculations require from 1 to 2 hours on the fastest computer available today (IBM 360-91). Three-dimensional calculations would require an order of magnitude more time. The axial symmetry imposed on the problem is not too restrictive for Reynolds numbers up to about 200. Experiments show that the major characteristics of the flow field of a uniform flow past a thin disk remain axisymmetric up to that Reynolds number.[1] The omission of all three-dimensional disturbances makes it possible to obtain stable solutions even for Reynolds numbers higher than 200 (in our case, 300 and 600), but the physical significance and meaning of these solutions are not clear. This makes the study of the effect of three-dimensional disturbances on the physical stability of axisymmetric flow fields all the more interesting. There are some interesting questions in this regard. Is there a lower or an upper limit to the Reynolds number under which such disturbances will grow? Is there any physical validity to axisymmetric solutions for high Reynolds numbers? Such questions can be answered only by repeating the calculations with a three-dimensional model; this, however, is impossible at present.

Because we want to achieve solutions for Reynolds numbers as high as possible and because some of the phenomena which we are trying to model are time-dependent, we used a temporal approach, i.e., we formulated the problem as an initial-boundary-value problem. The initial and boundary conditions will be discussed in a later section.

Once axial symmetry is imposed, we can define a Stokes stream function which will satisfy the continuity equation automatically. This is the greatest advantage of the vorticity-stream function formulation. If the primitive variables $\vec{u}$, P are used, special care has to be taken to satisfy the continuity equation as accurately as possible. But it must be pointed out that the vorticity-stream function approach works very nicely and simply only in the two-dimensional or axisymmetric cases. A vector potential must be used in three dimensions and the problem becomes considerably more complicated.

Because of the symmetry, the only vorticity component that survives is the one perpendicular to the meridian plane. This component will be designated by ω. The vorticity transport equation written for this component in cylindrical polar coordinates r, ϕ, z becomes

$$\frac{\partial \omega}{\partial t} = -\left[\frac{\partial (\omega u)}{\partial z} + \frac{\partial (\omega v)}{\partial r}\right] + \nu\left[\nabla^2 \omega - \frac{\omega}{r^2}\right] \qquad [5]$$

where u and v are the velocity components in the z- and r-directions, respectively. These velocity components expressed in terms of the stream function ψ are:

$$u = -\frac{1}{r}\frac{\partial \psi}{\partial r} \; ; \qquad v = \frac{1}{r}\frac{\partial \psi}{\partial z} \tag{6}$$

If we use Equation [6] in the definition of the vorticity, we get

$$\omega = \frac{1}{r}\left[\nabla^2 \psi - \frac{2}{r}\frac{\partial \psi}{\partial r}\right] = \frac{1}{r} D^2 \psi \tag{7}$$

where D^2 is an operator relating the vorticity and the stream function.

The cylindrical polar coordinate system is natural for axisymmetric problems, but the family of obstacles that are of interest here, namely disks of various thicknesses, can be better represented by the oblate-spheroidal system η, θ, ϕ. This system consists in the meridian plane of ellipses of η = const and hyperbolas of θ = const. Our obstacle was chosen to be the interior of an ellipse $\eta = \eta_b$ which is rotated around the axis of symmetry (see Figure 1).* The relation between the two coordinate systems is given by:

$$r = a \cosh \eta \sin \theta, \qquad z = a \sinh \eta \cos \theta \tag{8}$$

where a is the distance of the focal point of the ellipses from the centerline. The governing equations were transformed to the oblate-spheroidal system but the u, v components of the velocity were retained. This was done because of the clear physical meaning of u and v. Results are interpreted more easily in terms of u, v rather than in terms of the velocity components in η, θ, the directions of which vary from point to point.

We also nondimensionalized all physical variables by the length a, by the uniform velocity at infinity in the z-direction U, and by the density ρ or a suitable combination of them. Therefore, the nondimensionalization was carried out by:

$$r = \frac{r'}{a} \; ; \quad z = \frac{z'}{a} \; ; \quad u = \frac{u'}{U} \; ; \quad v = \frac{v'}{U} \; ; \quad t = \frac{t'}{a/U}$$

$$\omega = \frac{\omega'}{U/a} \; ; \quad P = \frac{P'}{\rho U^2} \; ; \quad \tau = \frac{\tau'}{\rho U^2} \; ; \quad \psi = \frac{\psi'}{U \cdot a^2} \tag{9}$$

where the primes indicate the physically dimensioned variables.

By applying the nondimensionalization Equation [9] and the transformation Equation [8] to Equations [5], [6], and [7] we arrive at the governing set of equations:

---

*Graphical and tabular material is placed at the end of the text.

The vorticity-transport equation:

$$c\frac{\partial\omega}{\partial t} = -\left[\cosh\eta\cos\theta\left(\frac{\partial}{\partial\eta}(\omega u)+\frac{\partial}{\partial\theta}(\omega v)\right)+\sinh\eta\sin\theta\cdot\left(\frac{\partial}{\partial\eta}(\omega v)-\frac{\partial}{\partial\theta}(\omega u)\right)\right]+\frac{2}{R_e}\left[\frac{\partial^2\omega}{\partial\eta^2}+\frac{\partial^2\omega}{\partial\theta^2}+\tanh\eta\frac{\partial\omega}{\partial\eta}+\cot\theta\frac{\partial\omega}{\partial\theta}-\frac{\omega\cdot c}{\cosh^2\eta\sin^2\theta}\right] \quad [10]$$

The velocity components definition in terms of ψ:

$$u = \frac{-1}{\cosh\eta\sin\theta\cdot c}\cdot\left[\sinh\eta\sin\theta\frac{\partial\psi}{\partial\eta}+\cosh\eta\cos\theta\frac{\partial\psi}{\partial\theta}\right]$$

$$v = \frac{1}{\cosh\eta\sin\theta\cdot c}\cdot\left[\cosh\eta\cos\theta\frac{\partial\psi}{\partial\eta}-\sinh\eta\sin\theta\frac{\partial\psi}{\partial\theta}\right] \quad [11]$$

The definition of ω in terms of ψ:

$$\omega = \frac{1}{\cosh\eta\sin\theta\cdot c}\cdot\left[\frac{\partial^2\psi}{\partial\eta^2}+\frac{\partial^2\psi}{\partial\theta^2}-\tanh\eta\frac{\partial\psi}{\partial\eta}-\cot\theta\frac{\partial\psi}{\partial\theta}\right] \quad [12]$$

Here $R_e = 2Ua/\nu$ is the Reynolds number based on the focal diameter (the distance between the two focal points of the body ellipse which is not equal to the outer diameter), and $c = \cosh^2\eta - \sin^2\theta$ is the nondimensionalized metric coefficient of the η and θ coordinates. Equations [10] and [12] are two equations in two unknown scalar functions ω and ψ. Equation [11] is an auxiliary equation determining u and v which appear in Equation [10].

The vorticity-stream function formulation has one more advantage which is rather a blessing in disguise, namely it eliminates the pressure from the solution. Indeed, if one is not interested in the pressure, one can proceed with the solution and obtain the vorticity, stream function, and velocity fields without solving for the pressure at all. However, the pressure is an essential variable, and one would like to evaluate the pressure at least on the obstacle itself so that the pressure drag coefficient may be calculated. (There is no lift in our case.) As described in detail in a previous work,[10] the retrieval of the pressure field from the known velocity field is not a trivial matter. Fortunately, the pressure distribution on the centerline and on the obstacle can be found directly from the vorticity field.

On the centerline

$$V = \omega = \frac{\partial u}{\partial \theta} = \frac{\partial P}{\partial \theta} = 0$$

from the symmetry; thus, the momentum equation in the z-direction in nondimensional form reduces to:

$$\frac{\partial P}{\partial z} + u \frac{\partial u}{\partial z} = \frac{2}{R_e} \nabla^2 u - \frac{\partial u}{\partial t} \quad \theta = 0, \pi \qquad [13]$$

Taking $\partial/\partial z$ of the continuity equation, subtracting $\partial\omega/\partial r$ and ω/r, and using the symmetry condition, we arrive at:

$$\nabla^2 u \Big|_{\theta=0} = -\left(\frac{\partial \omega}{\partial r} + \frac{\omega}{r}\right) \qquad [14]$$

On the centerline, both $\omega = r = 0$ and a limiting process yields:

$$\nabla^2 u \Big|_{\theta=0} = -2 \frac{\partial \omega}{\partial r}$$

Using this in Equation [13] and integrating from $\eta = \eta_b$ (which is the front stagnation point where $P = P_0$ and $u = 0$) to the free stream region (where $P = 0$ and $u = -1$), we obtain the stagnation pressure as:

$$P_0 = \frac{1}{2} + \int_{\eta=\eta_b}^{\eta=\infty} \left(\cosh \eta \frac{\partial u}{\partial t} + \frac{4}{R_e} \frac{\partial \omega}{\partial \theta}\right) d\eta \qquad [15]$$

Note that the pressure at the free stream can be set to zero because the absolute level of the pressure is arbitrary. We can see that for steady inviscid flow, the stagnation pressure is that of the Bernoulli equation, i.e., $P_0 = 1/2$. The factor 1/2 comes from the nondimensionalization by ρU^2 rather than the usual $1/2\ \rho U^2$.

In order to get the pressure distribution on the obstacle itself, we first find $\partial P/\partial\theta$ by using the momentum equation in the θ-direction as given by Happel and Brenner (page 116 of Reference 13). On the obstacle $u = v = 0$, therefore, the slow-motion solution discussed there holds and we obtain:

$$\frac{\partial P}{\partial \theta}\Big|_b = \frac{2}{R_e} \cdot \left[\frac{\partial \omega}{\partial \eta} + \tanh \eta_b\, \omega\right] \qquad [16]$$

Upon integrating from the front stagnation point, we get:

$$P_b = P_0 + \int_0^{\theta} \frac{2}{R_e} \cdot \left[\frac{\partial \omega}{\partial \eta} + \tanh \eta_b \, \omega \right] d\theta \qquad [17]$$

Once the pressure distribution on the obstacle is determined, it can be integrated to give the drag coefficient as follows:

$$C_{DP} = \frac{D_P}{\frac{1}{2} \rho U^2 \cdot \pi a^2 \cosh^2 \eta_b} = \int_0^{\pi} \frac{P_b' \cdot \cos \alpha \cdot dA}{\frac{1}{2} \rho U^2 \cdot \pi a^2 \cosh^2 \eta_b}$$

$$= 4 \int_0^{\pi} P_b \cos \theta \sin \theta \, d\theta \qquad [18]$$

where α is the angle between the normal to the surface and the z-axis and P_b' is the dimensional pressure on the surface. The differentiations and integrations of Equations [15], [17], and [18] are performed numerically to obtain the pressure distribution on the obstacle and the pressure drag coefficient.

The friction drag and drag coefficient can be found directly from the vorticity distribution. It can be shown that the shear stress is exactly $\mu \cdot \omega_b'$ on the surface of the obstacle and that therefore the friction drag coefficient is:

$$C_{DF} = \frac{D_F}{\frac{1}{2} \rho U^2 \cdot \pi a^2 \cosh^2 \eta} = \int_0^{\pi} \frac{\mu \cdot \omega_b' \cdot \sin \alpha \, dA}{\frac{1}{2} \rho U^2 \cdot \pi a^2 \cosh^2 \eta}$$

$$= \frac{8}{R_e} \tanh \eta_b \int_0^{\pi} \omega_b \cdot \sin^2 \theta \, d\theta \qquad [19]$$

where again ω_b' is the dimensional vorticity on the surface and the integration of Equation [19] is carried out numerically.

INITIAL AND BOUNDARY CONDITIONS

As explained before, the problem was formulated as an initial-boundary-value problem. Therefore, we have to specify an initial solution at time $t = 0$ and boundary conditions on all boundaries for all subsequent times. Since it is the initial and boundary conditions associated with the system of differential equations which single out a solution from a large family of possible solutions, great care must be exercised when specifying those conditions.

In interpreting the results as well as comparing them with experiments, we must take into account the fact that the boundary conditions used here do not always correspond precisely to those existing in the experimental setup.

In specifying an initial solution, we may distinguish three essentially different possibilities. The first is to start from a fluid at rest, i.e., $u = v = 0$ everywhere. The second is to specify $\omega = 0$ everywhere, i.e., a potential flow field as an initial solution. The third is to start from a slow motion solution (either Stokes or Oseen) when such solutions are known for the specified geometry. We have chosen the second approach because it is closest to an impulsive-start condition and, in some cases, involves the least work in reaching a steady state, if one exists.

The no-flow condition is too far removed from the steady-state condition and therefore will require much more work. The third approach might be more beneficial for low Reynolds numbers where the final solution is very close to a slow-motion solution. However, we used the potential field as an initial solution even for $R_e = 10$ for the sake of uniformity in the formulation and in order to investigate the behavior of the separation in the back of the disk.

When specifying the boundary conditions, we are faced with one of the greatest difficulties of the whole procedure. To begin with, we would like to obtain the solution of the flow past an obstacle in an infinite medium, i.e., $U = -1$, $v = 0$ (the undisturbed flow) is prescribed at infinity. However, the necessity for constructing the solution on a finite grid dictates the specification of the boundary conditions on a finite field. In a sense, the incompressible external flow problem is not well defined; we need to know the solution we seek before solving the problem if we are to specify accurate boundary conditions on the outer boundary of the finite field. Under the circumstances, we look for approximate boundary conditions such that the effect of the approximation will be minimized inside the field. To achieve that, we must rely mainly on physical intuition and to some extent on heuristic arguments.

Various boundary conditions may be specified on the outflow region which is the most troublesome part of the boundary. A few of these possibilities are: (1) the linear extrapolation of ψ and ω; (2) the parallel flow condition, i.e., $\partial\psi/\partial z = 0$; and (3) the assumption that uniform flow is coming in and going out of the flow field. Condition (2) has been used successfully in the case of a sphere contained in a pipe.[10] However, the existence of a pipe line which is not a coordinate line considerably complicates the programming and necessitates a special weighted differentiation for points which are not grid points and for grid points adjacent to them. To avoid this complication, we preferred to make the outer boundary a coordinate line, i.e., a nearsphere ellipsoid with its axes about 20 radii of the disk (see Figure 1). A uniform flow was prescribed on this outer boundary. It is realized that such a boundary condition is exact only when the outer boundary is at infinity and that the approximation involved is the proximity of the boundary to the obstacle. In order to rate as satisfactory, although not ideal, the outer boundary must be at a sufficient distance from the obstacle to satisfy a heuristic consistency condition which is derived from physical intuition.

The temporal process which is taking place is that of convecting and diffusing the vorticity generated on the obstacle into the field. If the vorticity that has been transported to the outer region at any time is negligible, then the original assumption that the vorticity is zero at this distance, i.e., the uniform flow condition, is at least consistent. However, this does not constitute proof that the effect of using this boundary condition is negligible. More experiments with farther and nearer boundaries must be done to estimate this effect quantitatively.

All the other boundary conditions are relatively simple and straightforward. On the centerlines, we impose the symmetry condition $\omega = \psi = v = \partial u/\partial\theta = \partial P/\partial\theta = 0$. On the obstacle, we have the no-slip boundary condition, i.e., $u = v = \psi = 0$. We calculate the vorticity on the surface by second-order, one-sided differencing of the derivatives constituting the vorticity $\omega = \partial v/\partial z - \partial u/\partial r$. The accuracy of the calculation of the surface vorticity is very crucial since the whole problem is created by the generation of this vorticity and its transport in the flow field. There are indications that the high curvature at the edge of the disk has a considerable effect on the accuracy of the vorticity evaluation in that region. A special study is already underway to determine the most efficient and accurate method of calculating the vorticity on the surface. However, for the purpose of this study, straightforward finite differencing was used.

NUMERICAL METHODS

THE FINITE-DIFFERENCE SCHEME

The field of computation was defined on a grid composed of the intersections of the lines η = const and θ = const. The increments between lines were held constant at $h_\eta = 0.05$ and $h_\theta = \pi/30$. The constant spacing in η expanded the mesh size radially and accounted for the large density of grid points near the edge of the disk (see Figure 1b) where they are needed most because of the greater details required there. The boundaries of the field are $\theta = 0$ on the right part of the centerline, $\eta = \eta_b$ on the disk surface, $\theta = \pi = (JL - 1) \cdot h_\theta$ on the left part of the centerline, and $\eta = \eta_f = (IL - 1) \cdot h_\eta$ on the outer boundary. Here $IL = 75$ and $JL = 31$ are the ranges of the indices of the η and θ coordinates, respectively. With $IL = 75$, the approximate radius of the outer boundary is about 20 radii of the disk. The choice of this distance is based on experience with the sphere case.[10] However, many more points are used inside the field than were used with the sphere.

All the dependent variables ω, ψ, u, v, and P are defined on the mesh points of the grid. The implications of this definition on the conservation of mass was previously discussed.[10] On this grid, second-order accuracy central differencing is used for the spatial derivatives of the convective terms. Dufort-Frankel central time differencing was used for the time derivative and the viscous terms. This scheme is also of second-order accuracy both in time and in space. In addition it is unconditionally stable for the viscous terms alone

and, therefore, is believed to offer good numerical stability properties. This expectation did not materialize in the disk case, as will be discussed later. More details on a similar differencing scheme may be found in the sphere report.[10]

The governing equations in their finite-difference form are:

The vorticity-transport equation:

$$\omega_{i,j}^{n+1} = \left[c_{i,j} + \frac{4\delta t}{R_e}\left(\frac{1}{h_\eta^2} + \frac{1}{h_\theta^2} + \frac{c_{i,j}}{2\cosh^2\eta_i \sin^2\theta_j}\right)\right]^{-1}$$

$$\cdot \left\{ -2\delta t \left[\cosh\eta_i \cos\theta_j \left(\frac{(\omega u)_{i+1,j} - (\omega u)_{i-1,j}}{2h_\eta} + \frac{(\omega v)_{i,j+1} - (\omega v)_{i,j-1}}{2h_\theta} \right) \right.\right.$$

$$\left. + \sinh\eta_i \cos\theta_j \left(\frac{(\omega v)_{i+1,j} - (\omega v)_{i-1,j}}{2h_\eta} - \frac{(\omega u)_{i,j+1} - (\omega u)_{i,j-1}}{2h_\theta} \right) \right]$$

$$+ \frac{4\delta t}{R_e}\left[\frac{\omega_{i+1,j} + \omega_{i-1,j}}{h_\eta^2} + \frac{\omega_{i,j+1} + \omega_{i,j-1}}{h_\theta^2} + \tanh\eta_i \cdot \frac{\omega_{i+1,j} - \omega_{i-1,j}}{2h_\eta} \right.$$

$$\left. + \cot\theta_j \cdot \frac{\omega_{i,j+1} - \omega_{i,j-1}}{2h_\theta} \right] - \omega_{i,j}^{n-1} \cdot \frac{4\delta t}{R_e} \cdot \left(\frac{1}{h_\eta^2} + \frac{1}{h_\theta^2} + \frac{c_{i,j}}{2\cosh^2\eta_i \sin^2\theta_j} \right)$$

$$\left. + c_{i,j} \cdot \omega_{i,j}^{n-1} \right\} \qquad [20]$$

The vorticity-stream function relation:

$$\psi_{i,j} = \frac{1}{2\left(\frac{1}{h_\eta^2} + \frac{1}{h_\theta^2}\right)} \cdot \left[\frac{\psi_{i+1,j} + \psi_{i-1,j}}{h_\eta^2} + \frac{\psi_{i,j+1} + \psi_{i,j-1}}{h_\theta^2} \right.$$

$$- \tanh\eta_i \cdot \frac{\psi_{i+1,j} - \psi_{i-1,j}}{2h_\eta} - \cot\theta_j \cdot \frac{\psi_{i,j+1} - \psi_{i,j-1}}{2h_\theta}$$

$$\left. - \omega_{i,j} \cdot \cosh\eta_i \sin\theta_j \cdot c_{i,j} \right] \qquad [21]$$

The velocity in terms of the stream function:

$$u_{i,j} = \frac{-1}{\cosh \eta_i \sin \theta_j \, c_{i,j}} \cdot \left[\sinh \eta_i \sin \theta_j \cdot \frac{\psi_{i+1,j} - \psi_{i-1,j}}{2h_\eta} + \cosh \eta_i \cos \theta_j \cdot \frac{\psi_{i,j+1} - \psi_{i,j-1}}{2h_\theta} \right]$$

$$v_{i,j} = \frac{1}{\cosh \eta_i \sin \theta_j \, c_{i,j}} \cdot \left[\cosh \eta_i \cos \theta_j \cdot \frac{\psi_{i+1,j} - \psi_{i-1,j}}{2h_\eta} - \sinh \eta_i \sin \theta_j \cdot \frac{\psi_{i,j+1} - \psi_{i,j-1}}{2h_\theta} \right] \qquad [22]$$

The central time differencing cannot be used for the first time step or when the size of the time step is changed. Another equation corresponding to Equation [20] but with forward differencing in time was used for these special cases.

The calculational procedure is as follows:

1. Initialize the problem by selecting the field parameters and the Reynolds number.

2. Construct the initial solution by assuming $\omega = 0$ everywhere and solving for ψ iteratively.

3. Find u and v from ψ and then by applying the no-slip condition $u = v = 0$ on the surface, calculate ω_b for $t = 0$.

4. Advance the vorticity by a time step on inner grid points by use of Equation [20].

5. Obtain a complete solution of the stream function by use of Equation [21] with an iterative procedure.

6. Determine u and v from ψ and complete the ω field by calculating ω_b with one-sided differencing of u and v on the surface.

7. Rotate the storage and return to Step 4.

At preselected time steps, the sequence is interrupted for calculating the pressure on the body, for printing output, and for recording the arrays on magnetic tape for plotting purposes or for the continuation of the problem. The problem is set to run for a prescribed number of time steps after which the results are examined and the question of continuing or terminating the problem is decided. The plotting is done with a Stromberg-Carlson microfilm recorder Model SC-4020 utilizing the same plotting program as in the sphere case,[10] with the necessary adaptations to the different coordinate system.

NUMERICAL STABILITY AND ACCURACY

The physical stability of the flow field and the effect of axial symmetry on it were already discussed earlier. Here we will deal with the numerical stability only. Numerical stability and accuracy are the major factors influencing the choice of the finite-differencing scheme. Once such a scheme is chosen, these factors determine the quality of the solution and the amount of effort needed to obtain it. Therefore, the importance of understanding the effects that these two aspects have on the calculation cannot be exaggerated. Unfortunately, no stability analysis for the complete system of finite-difference equations is known to the author. Also no error estimates or bounds can be found at present for this complex system. Therefore, we have to take an experimental (in the numerical sense) approach to determine the appropriate size of the time step for each Reynolds number and the largest possible Reynolds number for a given mesh size.

The shortcomings of the very common approach of splitting the system into convective and diffusion terms and then performing a linearized stability analysis have already been discussed in detail in the sphere report.[10] The conclusion there was that very small time steps must be used in order to achieve stability when there are very large gradients in the field. For the sphere case, the maximum nondimensional vorticity on the surface at $t = 0$ was about 72.0. Because of the very high curvature, the maximum nondimensional vorticity on the disk at $t = 0$ is much higher. For a disk of thickness $\eta_b = 0.05$, it is about 4500.0 and a staggering 16000.0 for a disk of $\eta_b = 0.02$ thickness. These figures indicate how much the stability restriction on the size of the time step is aggravated by the existence of extremely high curvature near the edge of the disk.

Nondimensional time steps as small as 0.00001 had to be used in the initial phase to prevent divergence. Later on, when the initial huge gradient is relaxed, higher time steps can be used. However, even near steady state very large vorticity gradients exist near the edge, as can be seen in Figure 11. These gradients restricted even the final time steps to be an order of magnitude smaller compared with those used in the sphere work.[10] For each Reynolds number, the time step was increased until the problem became unstable. Then it was lowered back into the stable region. Thus, upper and lower bounds were established for the maximum allowable time step. One such sequence is shown in Figure 2 where the drag coefficient C_D is plotted versus time for $R_e = 10$. We see that the scheme is stable for $\delta t = 0.00012$. When it is increased to 0.00015, divergence begins and then when it goes back to 0.000125, the oscillations die out. The results of these experiments are shown in Figure 3 where the boundary of the stability region is given for a disk of thickness $\eta_b = 0.05$. The striking feature of these results is the linear relation between the size of the experimental maximum stable time step and the Reynolds number.

There is a slight deviation from linearity at $R_e = 600$ where $\delta t = 0.0075$ would have to be a stable time step under strict linearity. However, after about 400 (!) time steps with $\delta t = 0.0075$, diverging oscillations started to show up. A reduction of the time step to

$\delta t = 0.0072$ kept the solution stable for all subsequent times. The Dufort-Frankel scheme was supposed to be unconditionally stable for the diffusion terms alone. These are the only terms multiplied by $1/R_e$. Therefore, we must conclude that this stability limitation is due to the interaction of the viscous and the nonlinear terms. Thus, the splitting method fails drastically to produce any meaningful prediction of the allowable time step. Subsequent experiments showed that the variation of curvature under constant R_e number also has a drastic effect on the stability limit. This will be discussed in a separate report.

Let us now examine the problem of accuracy. As stated in the previous section, the finite-difference scheme is carried to second-order accuracy, i.e., terms of order h^3 or h^4 and higher are neglected in the Taylor expansion of the dependent variables. We cannot estimate the total error introduced by this truncation, but we do know the form and nature of the truncated terms. Again, the size of the gradients of the dependent variables plays a decisive role in the accuracy of the scheme. Thus, accuracy and stability are closely interrelated.

In truncating the spatial first-order derivatives of the convective terms, we produce the so-called "numerical viscosity," i.e., terms which are proportional to the size of the mesh squared. These terms compete with the real viscous terms which are proportional to $1/R_e$. When R_e is large and the second-order derivatives of the velocity components are small, the "numerical" and the "real" viscosity terms may become comparable and spurious oscillations begin. This effect, which is directly connected to the relation between mesh size and R_e number, can be clearly seen at $R_e = 300$ (Figure 9a). Here the equal vorticity lines break into small noiselike loops outside the viscous region.

It can be demonstrated that at $R_e = 300$, all these irregularities are at a very low level of less than 1 percent of the maximum vorticity in the field. This is done by gradually increasing the minimum level of the equal vorticity lines that are plotted (see Figures 9a–9d). When R_e is raised to 600, the inaccuracies increase in intensity and size, as can be seen in Figure 6d, but the general flow field is still smooth, as demonstrated by the higher level equal-vorticity lines and the streamlines (Figure 5d). Even so, one must admit that at this R_e number, the accuracy of the solution is more qualitative than quantitative in nature.

The only remedy to this situation now known to the author is to decrease the mesh size for higher Reynolds numbers, at least in the region where these inaccuracies occur. Some authors have been able to avoid this problem by using one-sided differencing schemes of lower order accuracy. However, it is felt that this does not eliminate the problem but only disguises it. Because of the large numerical viscosity generated by such a low order accuracy scheme, the "nominal" Reynolds number claimed by the formal selection of one is, therefore, unrealistically high. Higher order rather than lower order differencing of the convective terms might provide some advantage in this respect. However, more work must be done before conclusions can be drawn on this point.

One other interesting aspect of the numerical accuracy is the round-off error introduced by the finite length of the numbers processed by the computer. When working on a computer

which has eight or more significant digits, one rarely encounters any problems of round-off error accumulation with the type of calculations we are performing. However, the IBM 360-91 has a single-precision word of about seven digits. When the first run of $R_e = 100$ was done with single precision and with less stringent accuracy in the iterative process, the stagnation pressure turned out to be quite chaotic, as can be seen in Figure 4. Repetition of the same calculations with double precision produced the smooth line which appears as the average line on that figure. Other dependent variables like ω and ψ were not affected so drastically, and the single and double precision results agreed to four figures. In the integration performed to evaluate the stagnation pressure, numerical differentiation of the vorticity near the centerline is involved. The vorticity is very small in this region and therefore very sensitive to numerical differentiation, resulting in limited accuracy.

THE ITERATIVE METHOD

The process of obtaining the stream function from a known vorticity distribution by an iterative method is the most time-consuming step in the calculations. It is estimated that about 80 percent or more of the computer time is spent on this step. Therefore, it is of cardinal importance to make the iterative method as efficient as possible to keep the calculation time within reasonable limits. Gauss-Seidel pointwise iteration with an overrelaxation factor of 1.5 was used in the work on the sphere[10] and was considered satisfactory. In that case, the existence of a noncoordinate boundary line (the pipe line) would make any other method impossible. For the disk problem, the ψ-array can easily be fitted into a rectangular matrix, and an alternating-direction line relaxation method can be used.

Prior to making the time-dependent calculation, an extensive set of experiments was made with the actual size of the matrix to determine the most effective method and the optimal overrelaxation parameter. In these experiments, the initial solution with $\omega = 0$ everywhere in the finite field was evaluated from a guessed solution. The guess-solution used was the uniform potential flow over the disk in an infinite medium as given by Lamb.[14] As expected, the results of the experiments showed that the alternating-direction line relaxation is much more efficient even with the added work needed for relaxing a full line at a time. Closely spaced overrelaxation factors were tested and $RF = 1.8$ was found to be optimal.

The line relaxation used will be demonstrated by a relaxation along an η-line (i = const). A corresponding process for the relaxation along the other coordinate can easily be derived along the same lines.

Equation [21] is rearranged to yield:

$$\psi_{i,j} = b\left[\left(\frac{1}{h_\theta^2} - \frac{\cot\theta_j}{2h_\theta}\right)\cdot\psi_{i,j+1} + \left(\frac{1}{h_\theta^2} + \frac{\cot\theta_j}{2h_\theta}\right)\psi_{i,j-1} + (EDER_{i,j} - Q_{i,j})\right] \quad [23]$$

where $b = \dfrac{1}{2\left(\dfrac{1}{h_\eta^2} + \dfrac{1}{h_\theta^2}\right)}$; $Q_{i,j} = \omega_{i,j} \cosh \eta_i \sin \theta_j \, c_{i,j}$ and $EDER_{i,j}$ are all the terms that are not on the relaxed line i = const.

$$EDER_{i,j} = \frac{\psi_{i+1,j} + \psi_{i-1,j}}{h_\eta^2} - \tanh \eta_i \, \frac{\psi_{i+1,j} - \psi_{i-1,j}}{2h_\eta}$$

On the line i = const, we can write a general formula:

$$\psi_{i,j} = G_j \, \psi_{i,j+1} + ST_{i,j} \qquad [24]$$

Since on the centerline, $\psi_{i,1} = 0$ for all i, we find from Equation [23] with $j = 2$ that

$$G_2 = d_2 \quad \text{and} \quad ST_{i,2} = b\,(EDER_{i,2} - Q_{i,2}) \qquad [25]$$

and for all subsequent j's, we derive the recursive formula:

$$G_j = \frac{d_j}{1 - e_j G_{j-1}} \qquad [26]$$

$$ST_{i,j} = \frac{1}{1 - e_j G_{j-1}} \cdot [e_j \cdot ST_{i,j-1} + b\,(EDER_{i,j} - Q_{i,j})]$$

where

$$d_j = b \cdot \left(\frac{1}{h_\theta^2} - \frac{\cot \theta_j}{2h_\theta}\right)$$

and

$$e_j = b\left(\frac{1}{h_\theta^2} + \frac{\cot \theta_j}{2h_\theta}\right)$$

To terminate the calculations of $ST_{i,j}$, we use the boundary condition $\psi_{i,JL} = 0$ for all i to get

$$ST_{i,JL-1} = \psi_{i,JL-1}$$

It can be seen from Equation [26] that the G_j's have to be calculated once only at the beginning of the program. Therefore, the relaxation involves the calculation of the $ST_{i,j}$ for $J = 2$ to $JL - 1$ and then substitution of these with the known G_j into Equation [24] to get the new ψ-values on the line. After this is done, the overrelaxation is applied by using:

$$\psi_{i,j}^{k+1} = \psi_{i,j}^{k} + RF \cdot (\psi_{i,j}^{k+1/2} - \psi_{i,j}^{k}) \qquad [27]$$

Here k is the iteration counter and $\psi^{k+1/2}$ is the newly calculated ψ-value before the overrelaxation is applied.

After the relaxation of the whole field in one direction is completed, a similar relaxation along the other direction is applied. The convergence is checked every five iterations in both directions by:

$$\frac{|\psi_{i,j}^{k+1} - \psi_{i,j}^{k}|}{EPSIL} - |\psi^{k}| \leq 0 \qquad [28]$$

for all i and j. This requires the relative error at any point to be less than a prescribed percentage which is governed by *EPSIL*. In our case, we used *EPSIL* = 0.0001, which corresponds to 0.01 of 1 percent.

The amount of iterations needed to achieve this accuracy depends on the R_e and the size of the time step; together, they determine the change in $\omega_{i,j}$ over a time step. Because the permissible time step varies linearly with the R_e number as shown before, the number of iterations does not change drastically and is typically about 20–30 iterations in both directions. For the 2088 points we had to relax, this takes about 1 second on the IBM 360-91 computer.

NUMERICAL RESULTS

TIME DEPENDENCE

Before discussing the results, it is important to note that the field plots of ψ and ω in Figures 5 through 10 are only a small part of the field. This enables us to get more details in the region of interest around the disk.

Let us first examine the time dependence of the solutions. Despite the expectations, based on experimental evidence, that solutions for Reynolds numbers above 200 will be time-dependent, all the solutions showed an approach to a steady state. In the initial phase of the $R_e = 600$ solution, there are large oscillations of C_D with time. These oscillations cannot be regarded as a numerical instability inasmuch as their periods are much larger than the time step used. Whenever diverging oscillations occurred, the period was of the order of a time step. However, the amplitude of the oscillations decreased with time, and in the last portion of the calculations, the oscillations had almost died out. The solution is very near a steady state (see Figure 16).

It is believed that the oscillations are caused by the truncation errors discussed earlier. In the initial phase, the border between the viscous and the inviscid regions, where these errors are pronounced is very near the body, and the vorticity gradients are very large.

Consequently, the truncation errors, which are of larger magnitude at $R_e = 600$, affect the immediate vicinity of the disk and cause the oscillations in C_D. At a later time, the vorticity gradients are relaxed and the truncation errors are much smaller and further away from the disk, as can be seen in Figure 6d. This reduces the effect which these errors have on C_D, and the oscillations die out. As the R_e number decreases, the truncation errors decrease, as was mentioned previously. Therefore, no such oscillations are observed at $R_e = 300$ and below.

On the other end of the R_e number range, the solution for $R_e = 10$ was not carried all the way to a steady state. Nevertheless, the solution is clearly approaching a steady state, as can be seen in Figure 13. Here the pressure distribution on the disk is given for various times. The difference between the curves is becoming smaller, despite the larger increment in time. In addition, the general features of the curves do not change with time. As can be seen in Table 1, a total of 5000 time steps were used for $R_e = 10$. Because of the severe stability restriction on the size of the time step, this amounted to a final time of only $t_L = 0.56715$. The other cases for $R_e = 100$, 300, and 600 were run to $t_L = 4.8136$, $t_L = 11.0822$, and $t_L = 16.7041$, respectively, with fewer time steps. Advancing the solution corresponding to $R_e = 10$ to a steady state with the present restrictions would exceed even the great capabilities of the IBM 360-91 computer.

It is felt, however, that as far as the behavior of the flow at $R_e = 10$ is concerned, the solution has reached an adequate state. As demonstrated by Figure 13, the main features of the flow do not change much any more. The remainder of the approach to a steady state will produce only very small changes in the flow field and will not teach us much more about the flow processes that are taking place. For these reasons, the solution was not continued beyond $NTS = 5000$, which took about 2 hours on the IBM 360-91 computer. The final result, as expected, would be a somewhat smaller C_D, which will be closer to the experimental value (see Figure 17), a smaller maximum vorticity (see Figure 11), smaller peaks of pressure (see Figure 12), and a small increase in the size of the separated region behind the disk (see Figure 5a).

The complete time dependence of the flow at $R_e = 300$ (both equal-vorticity lines and streamlines) and at $R_e = 600$ (equal-vorticity lines only) may be observed from a movie prepared from the results of this study. A representative selection of plots at various times are presented for $R_e = 300$ in Figure 7 (streamlines) and Figure 8 (equal-vorticity lines). There is no separation up to $t = 0.0112$ at $NTS = 130$; at this time, ψ first becomes negative at $j = 18$ or $\theta = 102$ deg, which is two grid points away from the edge $\theta = 90$ deg (see Figure 7a). The separated region then develops near the edge and bulges radially. This growth involves an increase in size both towards the edge and away from the edge (see Figure 7b). At this stage, the separation point on the edge side nearly attains its final value. Only then does the inner separation point start moving rapidly towards the centerline, accompanied by a radial increase of the separated region (see Figure 7c). After the separation point reaches the centerline, the separated region starts growing in the lateral direction until it reaches its

final shape (see Figures 7d–7f). This separation process is invariably the same for all R_e numbers and is in marked contrast to what happens with respect to the sphere.[10] There the separation always starts on the back of the sphere at the centerline. Then it climbs very fast on the surface, followed by a lateral growth to the final shape (see Figures 18 and 19 of Reference 10). In the case of the sphere, we never have a toroidal-shaped separation region as in the case of the disk, and the separated region is always like a bulge behind the sphere.

Figure 8 describes the development of the equal-vorticity lines with time. In the initial phase, all the vorticity is concentrated around the disk and is symmetric (see Figure 8a). Then as the convection starts affecting the vorticity transport, the lines are stretched in the outflow direction and squeezed in front of the disk (see Figure 8b). Already at this time, we can see the truncation effects building up on the border of the viscous region. This buildup becomes more and more pronounced as time increases (see Figures 8c–8f).

At the same time, the establishment of a local maximum can be detected in the vorticity field behind the disk. This local maximum is seen as a separated loop of an equal-vorticity line in the middle of the wake. As time passes, the vorticity is being diffused and convected downstream, resulting in a decrease of the general vorticity level in the field. This causes the separated equal-vorticity loop to shrink until it disappears completely. At this stage, the next lower level starts closing on itself until it separates from the line attached to the body. Such a separation of an equal-vorticity line is shown in Figure 8c, and its subsequent shrinking appears in Figures 8d and 8e. In Figure 8f the separated level of the previous plots has completely disappeared, and the next lower level is not high enough to show a completely closed loop. However, the local maximum exists, and its location is close to the center of the streamlines. No such separated loops or a local maximum were found at or below $R_e = 100$.

We see the same phenomenon at $R_e = 600$. But there is an additional separated loop at the rear end of the wake (as is shown in the movie, but not here). As much as we would like to interpret this loop as a vorticity shedding, the time sequence suggests that it is a result of the distortion of the equal-vorticity lines in the initial phase by the large truncation errors existing then. For both $R_e = 300$ and $R_e = 600$, there is no detachment of the streamlines. The final shape of the streamlines consists of smooth loops contained in a pocket behind the disk.

On the other hand, the separated loop of the equal-vorticity line in the middle of the viscous region cannot be attributed to the truncation errors because it occurs at a fairly high level of vorticity inside the wake. However, it cannot be interpreted as vorticity shedding because (1) there is no detachment of the streamlines and (2) it becomes a steady feature of the wake whereas the vorticity shedding is a periodic phenomenon. As far as the author knows, this feature of a separated local vorticity maximum inside the wake of an axisymmetric body at high Reynolds numbers is a new result and has not previously been reported in the literature.

Thus, on the basis of the present results and the previous results for the sphere, we are led to believe that no vorticity shedding occurs in strict axisymmetric flow fields, even for moderately high Reynolds numbers. The experimental shedding of "horseshoe" vorticity rings reported for both freely falling disks and spheres[1, 3, 11] must, therefore, be of three-dimensional nature and origin. Since the periodic shedding was reported only for freely falling objects, it might also be that it is associated with the freedom of the object to wobble and rotate around its own axis. No such freedom is allowed in the present numerical experiments where the position of the obstacle is fixed.

REYNOLDS-NUMBER DEPENDENCE

The discussion of Reynolds number dependence is based on results for the steady state of the various R_e number solutions. In this respect, the $R_e = 10$ solution is not complete, but in view of the discussion in the last section, we will regard the features of the flow field as qualitatively representing the steady state.

Figure 5 shows the streamlines for the various R_e numbers. The separation point for $R_e = 100$ and above is so extremely close to the edge as to be considered at the edge for all practical purposes. At $R_e = 10$, it is one grid point away from the edge at $\theta_s = 96$, but in the physical plane, it is such a small distance that it cannot be detected in the plot. Michael[12] shows that the separation point at $R_e = 8$ and $R_e = 30$ is considerably below the edge. It is the experience of the author that making the disk thinner brings the separation point nearer to the edge and not away from it. Therefore, it seems that this feature in Michael's results is due to inaccurate handling of the edge. The large variation of the separation point with R_e number in the sphere problem (see Figure 24 of Reference 10) is eliminated here by the large curvature, which dictates separation very near the edge of the disk. The effects of variation in thickness on the separation will be discussed in a separate report.

There are no experiments which measure the geometrical properties of the disk wake. Therefore, it is not possible to make quantitative comparisons of the geometrical configuration of the wake with physical data, as was done for the sphere. However, Reference 1 showed good qualitative agreement of the streamlines with the dye picture at $R_e = 100$. As expected, the radial size and the extent of the wake grow as the R_e number increases.

Figure 6 shows the equal-vorticity lines in the flow field for various R_e numbers. Here the role of convection in the transport of vorticity is clearly demonstrated. There is a small separated region behind the disk at $R_e = 10$, but the lines are still almost symmetric fore and aft. As the R_e number grows, the convection becomes larger in comparison with the diffusion, and the lines are stretched in the downstream direction and squeezed on the upstream side. This brings the practically inviscid region closer and closer to the front of the disk, and builds up a thin boundary layer which is a region of high vorticity. The boundary layer buildup is also supported by the pressure distribution of Figure 12, as will be discussed later.

Figure 11 shows the vorticity distribution on the disk for various R_e numbers. The large effect of high curvature on the flow field is seen clearly here. When we compare this figure with the corresponding one for the sphere (see Figure 27 of Reference 10) the striking differences that stand out are the steep gradient of the vorticity near the edge of the disk and the comparatively small change in the maximum vorticity on the disk. The lines are smooth and vary slowly in the case of the sphere, but there is a very sharp drop for the disk near the edge from large positive vorticity to low negative vorticity over an extremely small distance. This small separation of the maximum and the minimum of the vorticity is dictated by the inability of the fluid to negotiate such a high curvature. As a result, separation occurs very close to the edge, as shown earlier in the streamline plots.

A steep gradient contributes to a loss of accuracy in any numerical scheme. Here it becomes even more of a problem because of the stability restrictions it creates, as discussed earlier. It also demonstrates the absolute necessity for an extremely fine grid in such a region if gross errors are to be avoided. Such a grid was obtained here by the use of a coordinate system naturally fitted to the problem, i.e., the oblate spheroidal system. It is doubtful whether one can secure adequate resolution in this region with any other coordinate system.

For the sphere, the variation of the maximum vorticity on the surface ranged from $\omega_{max} = 3.3153$ for $R_e = 10$ to $\omega_{max} = 29.4549$ for $R_e = 1000$, i.e., in about a 10-to-1 ratio. For the disk, on the other hand, the variation is only between $\omega_{max} = 46.7667$ and $\omega_{max} = 53.679$ over the range of $R_e = 10$ to 600. This again is believed to be caused by the large curvature which necessitates sharp fluid turning and results in high vorticity even at low R_e numbers.

The increase of vorticity in the recirculatory portion of the surface (back part), which resulted in a secondary separation at $R_e = 1000$ for the sphere, is also obvious here. However, the intensity of the recirculating motion at $R_e = 600$ is not quite enough to cause a secondary separation. It might be that the lack of curvature on the back does not cause an adverse pressure gradient and, therefore, secondary separation will not occur even for higher R_e numbers.

Figure 12 describes the pressure distribution on the disk for various R_e numbers. Two very interesting features of the flow field are revealed here. The first is the different nature of the pressure distribution for low and high R_e numbers. The second is the breakdown of the boundary layer approximation near the separation point.

It was of great interest to find that at $R_e = 10$, the stagnation pressure is the lowest pressure on the front surface of the disk. From the stagnation point, the pressure rises slowly at first and then quite steeply to form a peak near the edge. Then it drops sharply to a minimum and rises again (see Figure 12). The validity of this strange distribution can be supported in a limiting sense with the help of Figure 14 and is explained in more detail by Figure 10. Figure 14 gives the distribution of $P_b \times R_e$ for $R_e = 10$ together with the limiting

case of the Oberbeck solution at $R_e = 0$. We see that the distribution corresponding to $R_e = 10$ possesses all the features we would expect it to have. On the one hand, it is very similar in shape to the solution corresponding to $R_e = 0$ but, on the other hand, it exhibits a slight asymmetry which is the result of the existence of finite convection. This asymmetry is demonstrated by the fact that the pressure dip in the back is lower than the peak in the front. Thus, the pressure distribution for $R_e = 10$ has a shape that is very likely to produce in the limit as $R_e \to 0$ the known Oberbeck solution shown here.

In contrast to that at $R_e = 10$, the stagnation pressure for $R_e = 100$ and above is the highest pressure on the front surface. The pressure decreases from the stagnation point to a minimum near the edge and then rises again.

The odd different behavior of the pressure for the low and high R_e numbers can be explained with the aid of Figure 10. As has been shown by Equation [16], the pressure gradient on the surface is governed mainly by the vorticity gradient normal to the surface. Figure 10 shows an enlargement of the equal-vorticity lines near the disk for various R_e numbers (only the upper half of the meridian plane is shown). Here we see that at $R_e = 0$, the equal-vorticity lines approach the surface almost tangentially. Thus, the normal derivative of the vorticity is positive at any point on the front surface, and the pressure rises towards the edge. At $R_e = 10$, the equal-vorticity lines are almost perpendicular to the surface at the lower part; this accounts for the very moderate increase of the pressure in that region. In the vicinity of the edge, the lines again become curled, with a positive normal derivative; this accounts for the steep rise toward the peak near the edge. For $R_e = 100$ and 300, the convective velocity parallel to the disk is large enough to cause the equal-vorticity lines to be swept upwards. This creates a negative normal derivative of the vorticity and causes the pressure to decrease from the stagnation point onward.

One more interesting point which is demonstrated by Figure 10 is the effect of the convection on the shape of the region of large vorticity gradient in the wake. This region is identified by the concentration of equal-vorticity lines at the back of the disk. At $R_e = 10$, this region is concentrated very near the edge. At $R_e = 100$, the region still emanates from the edge, but it is swept downstream and becomes a "boxlike" shape. At $R_e = 300$, one edge of the "box" is being pinched upward to create a pointed edge. The pinching is mainly caused by the convection associated with the recirculatory motion in the back of the disk and forms the "neck" which, in turn, causes the local-maximum loop to separate from the equal-vorticity line attached to the body. The absence of the neck at low R_e numbers explains why no local maximum of vorticity is found at $R_e = 100$ or below.

The breakdown of the boundary-layer approximation is clearly demonstrated by the pressure curves of $R_e = 100$, 300, and 600. We see that on the front part of the disk up to $\theta = 80$ degrees, the pressure distribution is almost the same for all these R_e numbers. This is in agreement with the result expected from a boundary-layer approximation. From that point on, however, there is a marked Reynolds-number effect on the pressure distribution. It is felt

that only the complete Navier-Stokes equations can give meaningful results in this region and in the viscous-wake region. If the boundary-layer equations could somehow predict the point beyond which they do not hold, there might be a way to artifically incorporate a boundary-layer and a finite-difference approach in the same field of computation. Such a combination is highly desirable since it would allow larger grid size and greatly reduce the amount of computation required for high Reynolds-number solutions. Nevertheless, it is interesting to see how with a fine mesh we can get all the different types of regions of the boundary layer, the viscous wake, and the inviscid outer flow combined in a natural unified way by the Navier-Stokes equations.

Figure 15 gives the stagnation pressure values for the various R_e numbers. No attempt was made to compare these with the results of an analysis similar to that of Homann.[15] It is felt that the Homann analysis, which agreed well with the results relating to the sphere for high R_e numbers (see Figure 30 of Reference 10), contains a boundary-layer-type approximation. Therefore, there is no point in comparing it with solutions of the complete Navier-Stokes equations, especially at low R_e numbers.

Finally, we show in Figure 17 the variation of the drag coefficient with the Reynolds number. The fact that the presently computed C_D for $R_e = 10$ is too high is probably caused by not reaching a steady state, as discussed before. At $R_e = 100$, the computed value agrees very well with the experimental values. This is the only R_e number carried to steady state where the conditions of the physical and numerical experiments are the same. As we advance to higher values of the R_e number, we see a rise in the experimental values of C_D and a decrease in the calculated ones. In his extensive paper,[3] Schmiedel claims that the rise which breaks the trend of the curve is associated with the appearance of periodic vorticity shedding at R_e numbers higher than 100. This explains the absence of such a rise in our results. With strict axial symmetry imposed on the flow, no vorticity shedding occurs. Therefore, no rise caused by the shedding can be observed.

CONCLUSIONS

The conclusions are divided into two categories, those pertaining to the numerical procedure and those dealing with the fluid dynamical aspects.

NUMERICAL PROCEDURE

1. The most important conclusion concerning the numerical method is that a high curvature of the obstacle has profoundly adverse effects on both numerical stability and accuracy. Even with the same mesh size in the mapped nondimensional plane, the high-curvature body requires a time step that is an order of magnitude smaller than that for a low-curvature body in order to achieve stability. This is due mainly to the very steep gradients of the vorticity in the field created by the high curvature. The same gradients also cause severe problems

with respect to loss of accuracy. In order to avoid large errors, an extremely fine mesh must be employed in the region of the large gradients, i.e., near the edge of the disk.

2. Another important aspect of the numerical scheme is the appearance of truncation errors or "numerical viscosity" on the border between the viscous and the inviscid regions. A finer mesh or an improved differencing scheme will have to be used to avoid this undesirable effect.

3. Sufficiently high precision must be maintained to prevent round-off errors. When the calculation was carried out with at most, seven significant digits, noiselike oscillations appeared in the pressure calculations. These oscillations disappeared when higher accuracy was employed.

4. Under the present restrictions, the calculation of the flow field around a body with high curvature requires a large (almost excessive) amount of computation. This amount increases considerably as the curvature increases and as the Reynolds number decreases. A more stable differencing scheme (probably an implicit one) may allow the use of larger time steps to alleviate some of the burden encountered here.

FLUID DYNAMICAL ASPECTS

1. The most important fluid-dynamical result is that no vorticity shedding was observed for the axisymmetric flow field around the disk, even for moderately high Reynolds numbers. All the solutions showed an approach to a steady state. By combining this with the absence of such shedding for the case of the sphere,[10] we can conclude that the shedding of vorticity is a three-dimensional effect, owing to three-dimensional disturbances.

2. The separation point is extremely close to the edge of the disk even for $R_e = 10$. This is achieved by use of a very fine mesh near the edge. Such a fine grid is missing in previous studies of flows around a disk or a sharp corner. In contrast to the first appearance of the separation on the sphere near the centerline, here the first separation appears near the edge. The shape of the separated region on the disk in the initial phase is a torus whereas on the sphere it is a solid bulge.

3. The different behavior of the pressure distribution on the disk for low and high Reynolds numbers is very interesting. For low Reynolds numbers ($R_e = 10$, for example), the stagnation pressure is the lowest pressure on the front of the disk, but for high Reynolds numbers ($R_e = 100$ and above), it is the highest pressure. This different behavior may have far-reaching implications for the nature of a flow around a singular point; this problem will be discussed in a separate report.

4. The existence of a local vorticity maximum inside the wake has been observed at the higher Reynolds numbers ($R_e = 300$ and 600) in the form of a closed loop of an equal-vorticity line. No such maximum was observed for $R_e = 10$ and 100. This maximum, which apparently

has not been reported before, is the result of the high convection in the recirculatory motion at high Reynolds numbers. In physical as opposed to numerical experiments, the axial symmetry cannot be preserved to such high Reynolds numbers, and the recirculatory motion is destroyed. This may explain why such a local maximum is revealed only in high Reynolds-number axisymmetric numerical solutions, which are presented here for the first time.

ACKNOWLEDGMENTS

The author thanks Dr. H. J. Lugt and Mr. C. W. Dawson for many stimulating discussions and valuable suggestions.

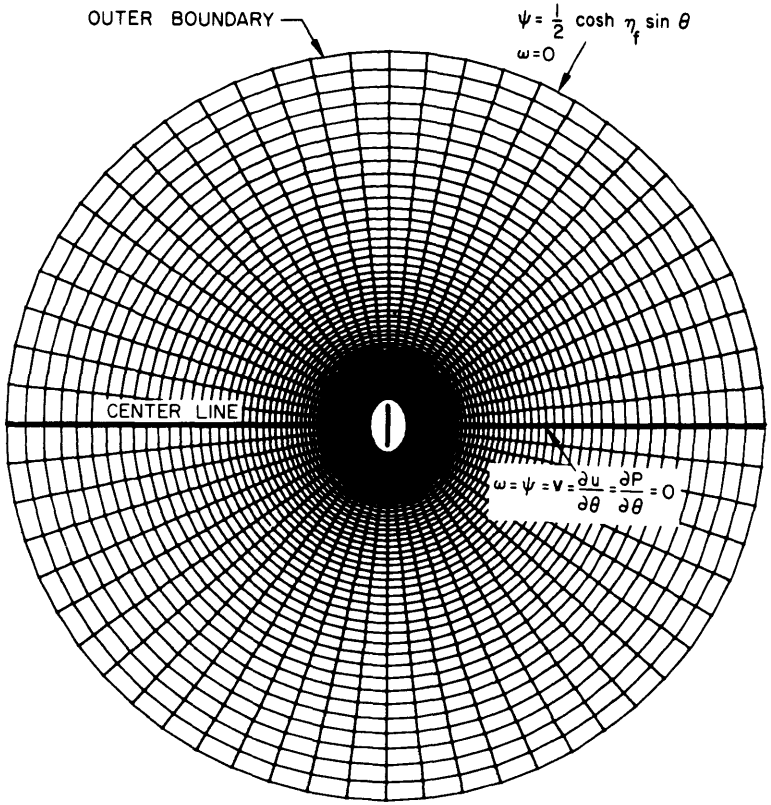

Figure 1a — The Outer Part of the Field

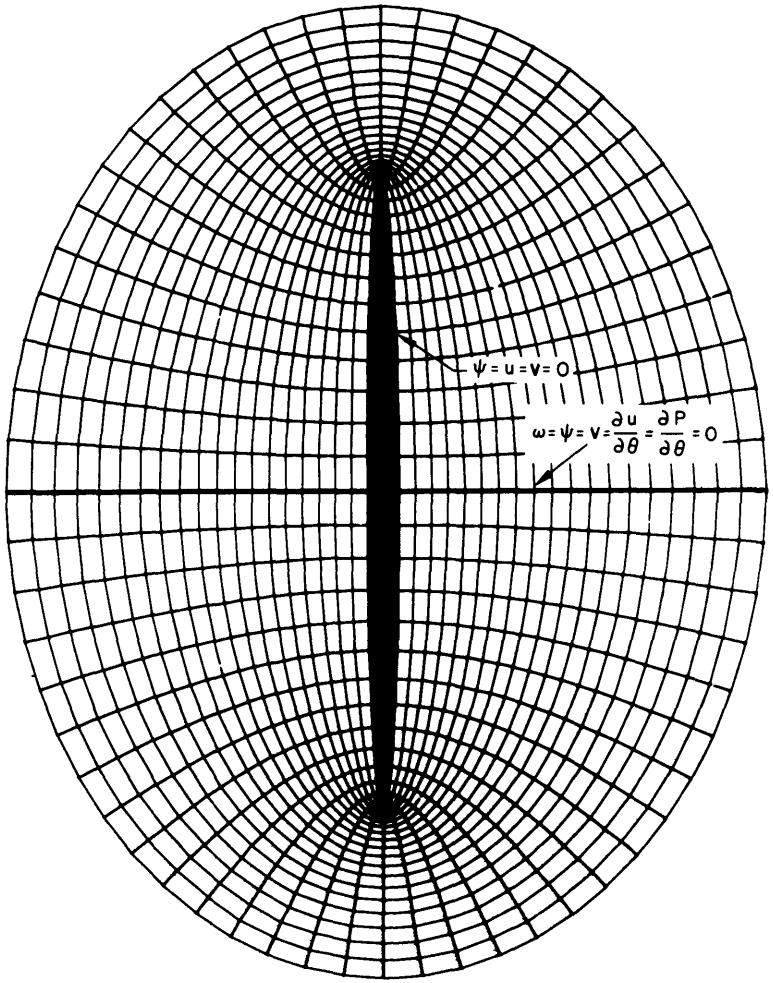

Figure 1b — An Enlargement of the Core Region near the Disk

Figure 1 — The Oblate-Spheroidal Grid in the Meridian Plane

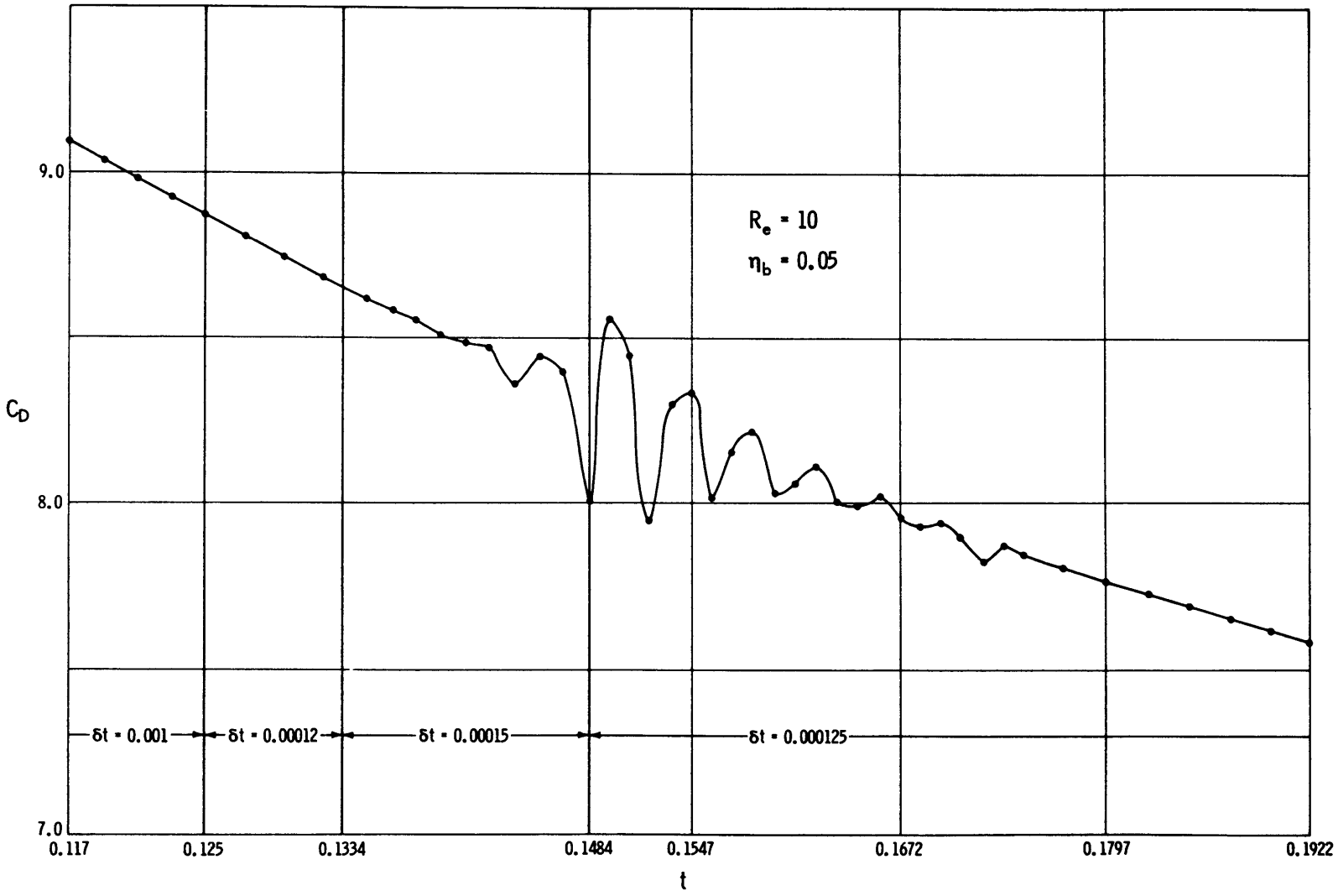

Figure 2 – A Stability Experiment at $R_e = 10$

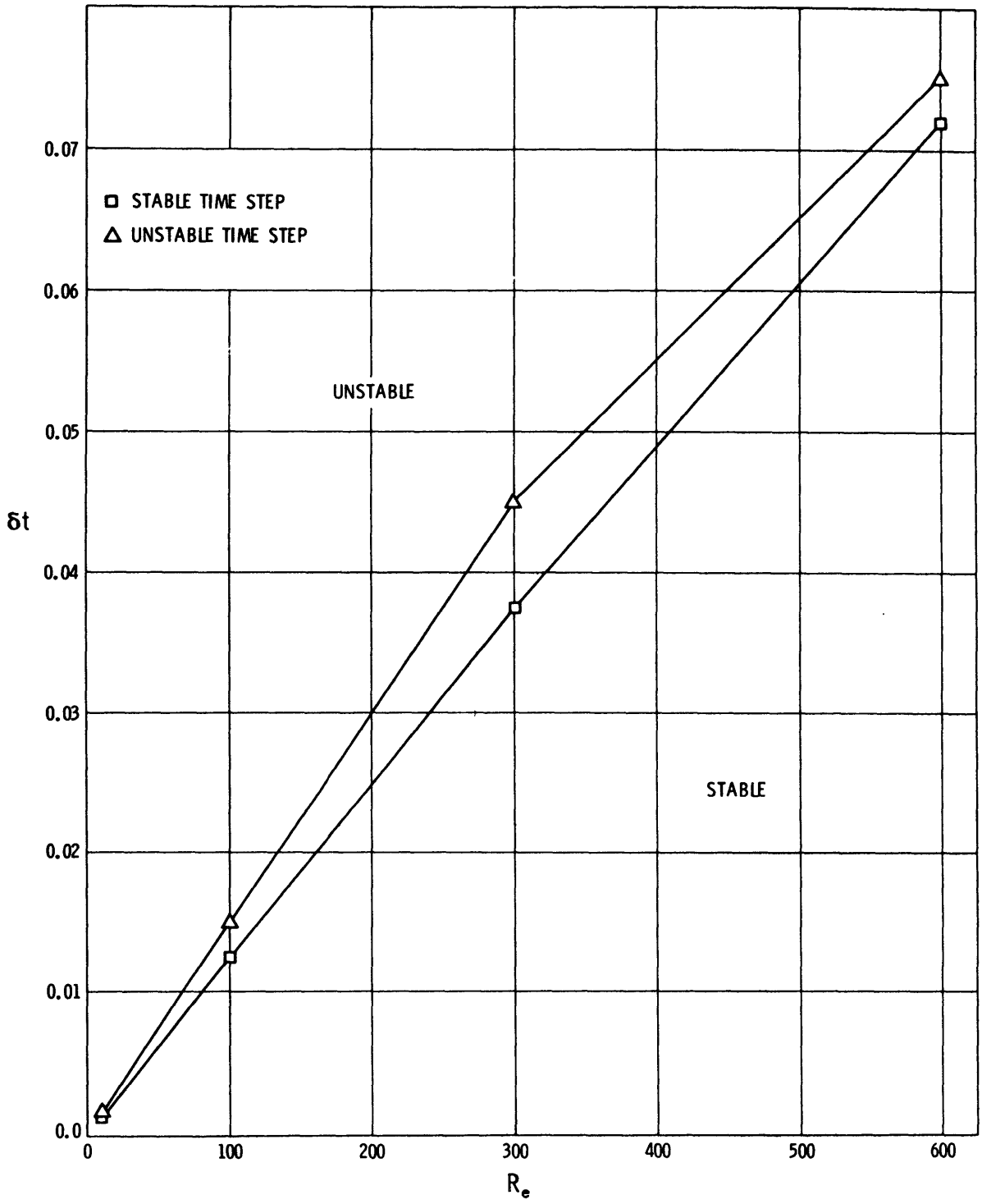

Figure 3 – Stability Region of a Disk with $\eta_b = 0.05$

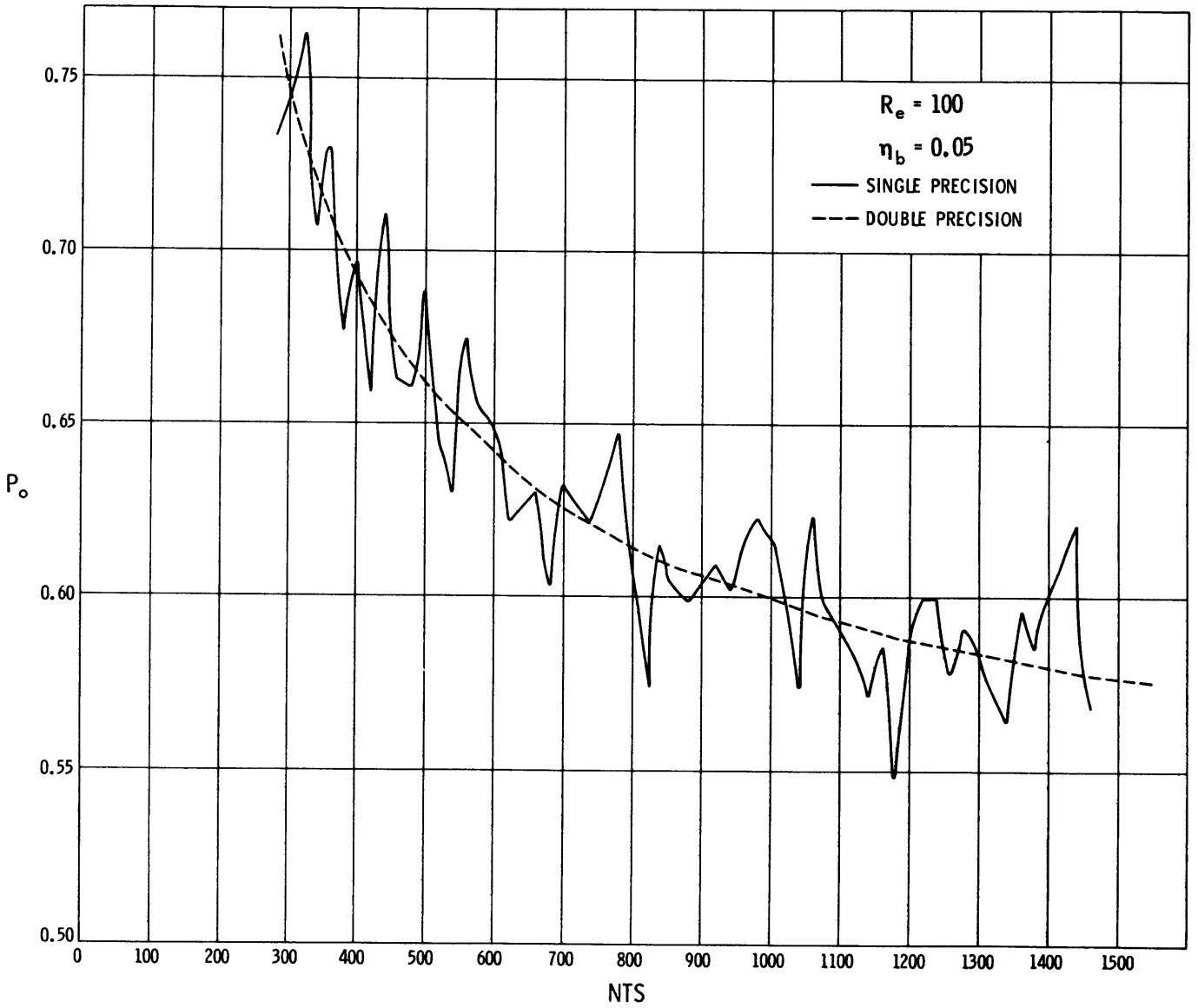

Figure 4 – The Effect of Round-Off Errors on the Calculation of the Stagnation Pressure P_0 at R_e = 100

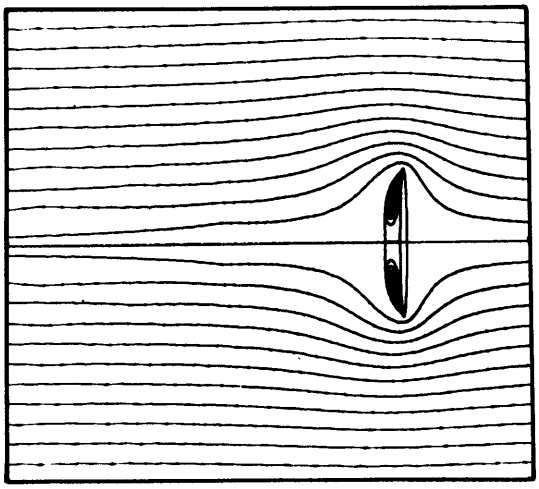

a. R_e=10 t=0.5672

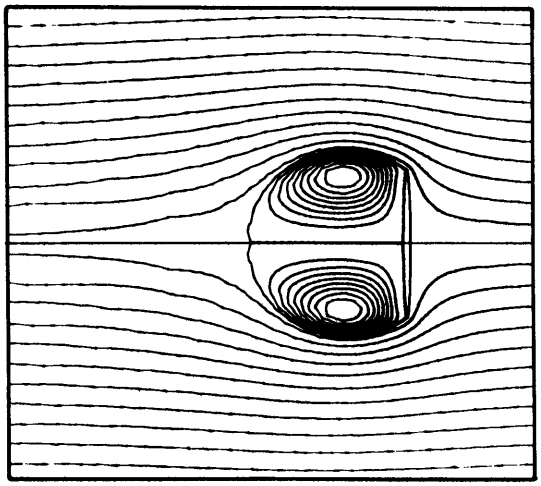

b. R_e=100 t=4.8136

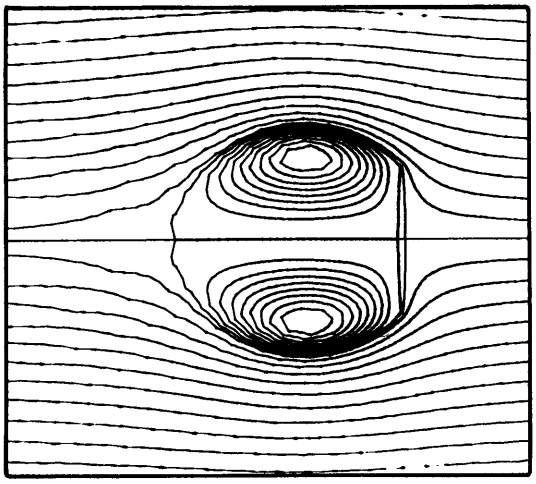

c. R_e=300 t=10.6822

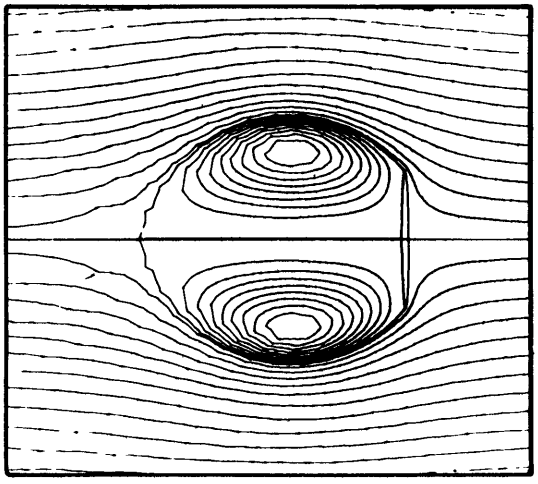

d. R_e=600 t=16.7041

Figure 5 – Late-Time Streamlines of a Disk in a Uniform Flow for Various Reynolds Numbers

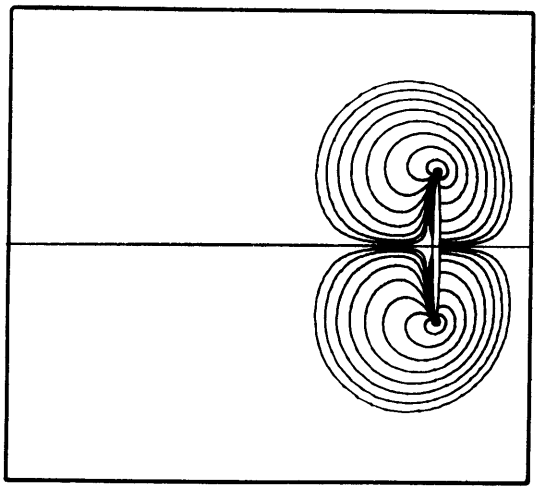

a. R_e= 10 t=0.5672

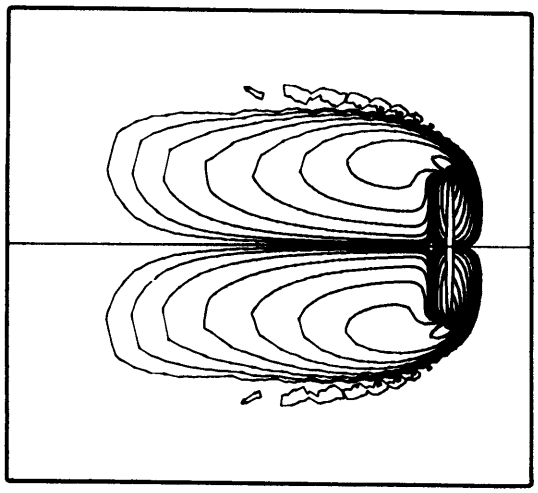

b. R_e= 100 t=4.8136

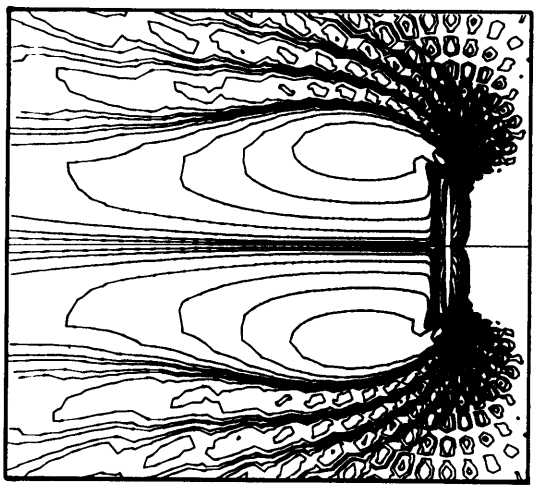

c. R_e= 300 t=10.6822

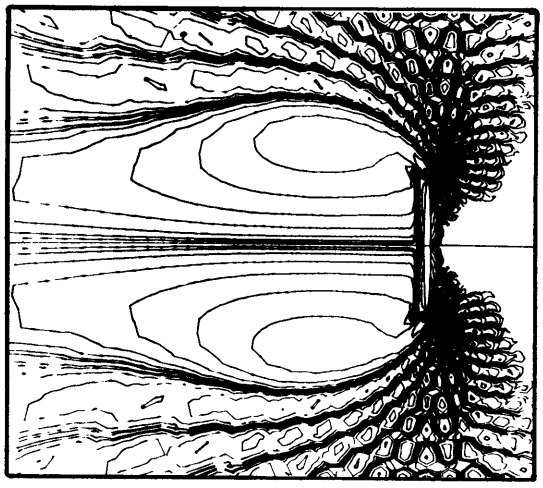

d. R_e 600 t 16.7041

Figure 6 – Late-Time Equal-Vorticity Lines of a Disk in a Uniform Flow for Various Reynolds Numbers

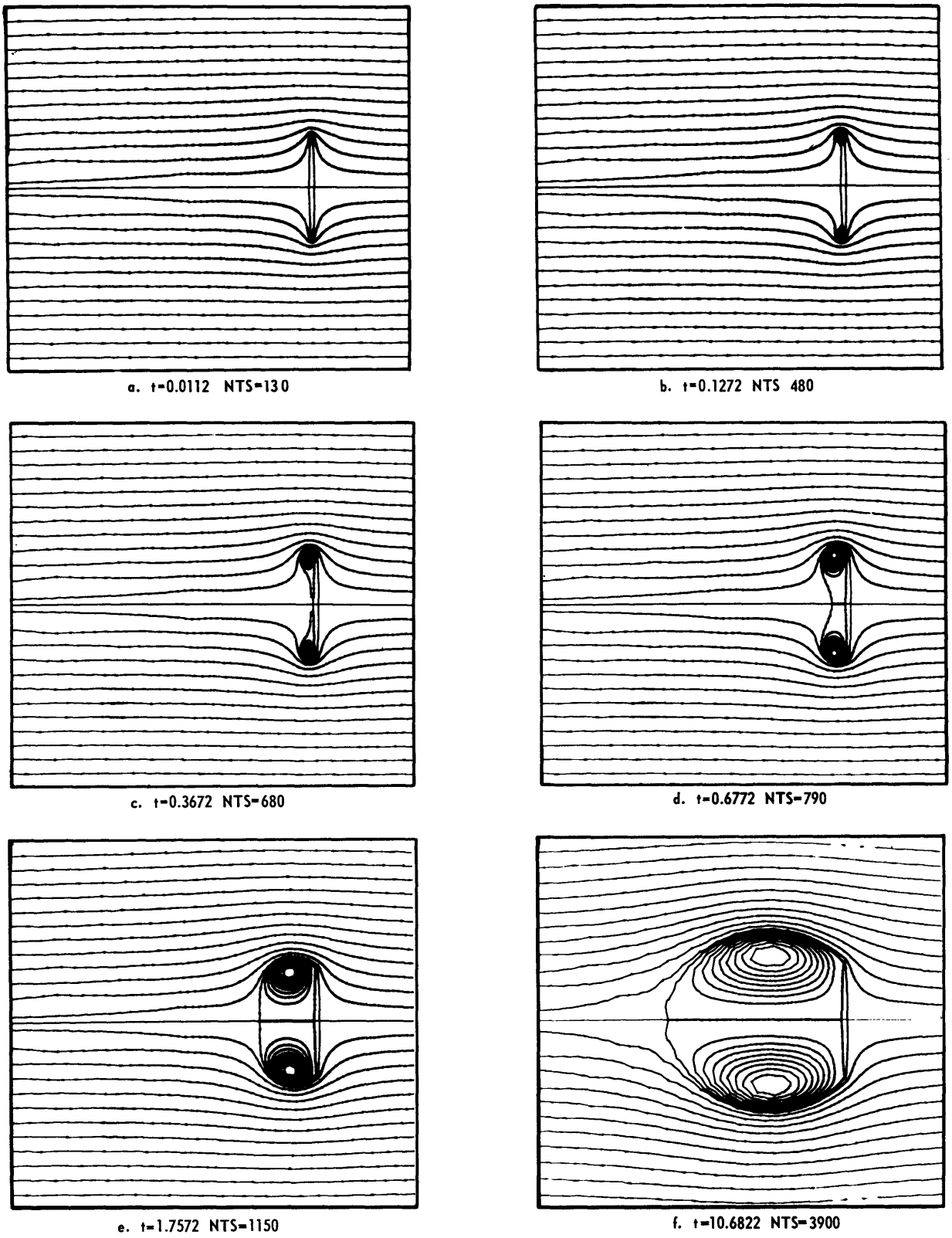

Figure 7 – Temporal Development of Streamlines of a Disk in a Uniform Flow at $R_e = 300$

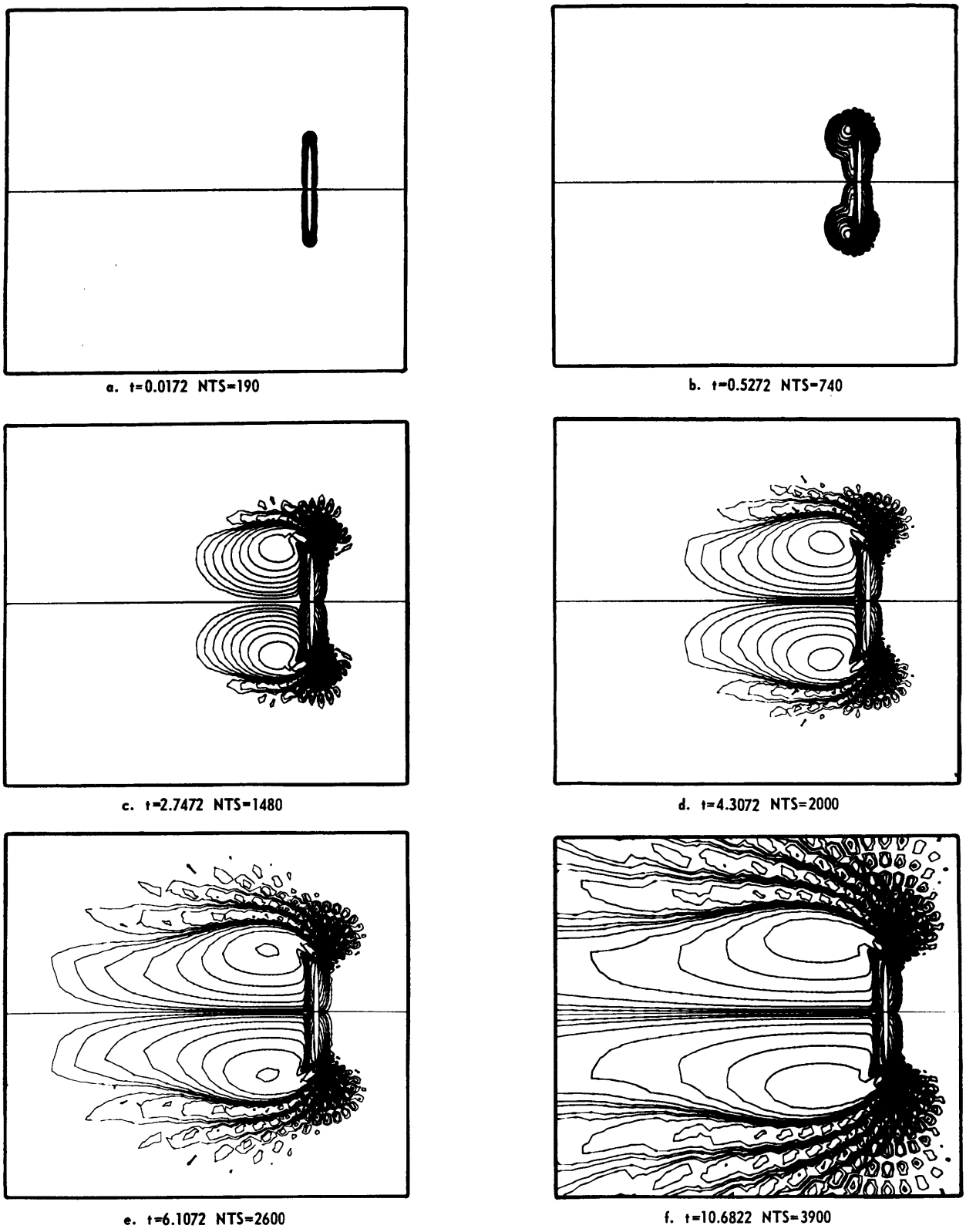

Figure 8 – Temporal Development of Equal-Vorticity Lines of a Disk in a Uniform Flow at $R_e = 300$

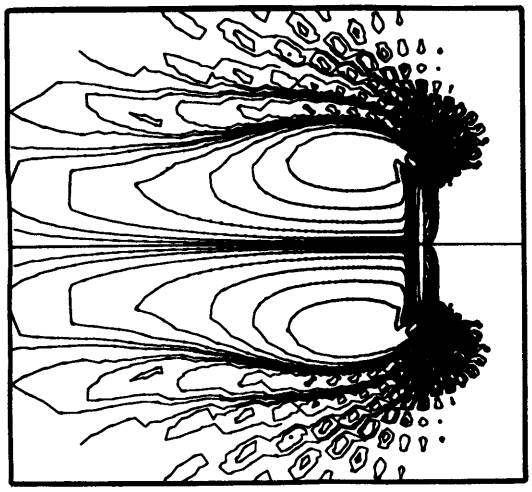

a. $C_{V\ min}$=0.03125

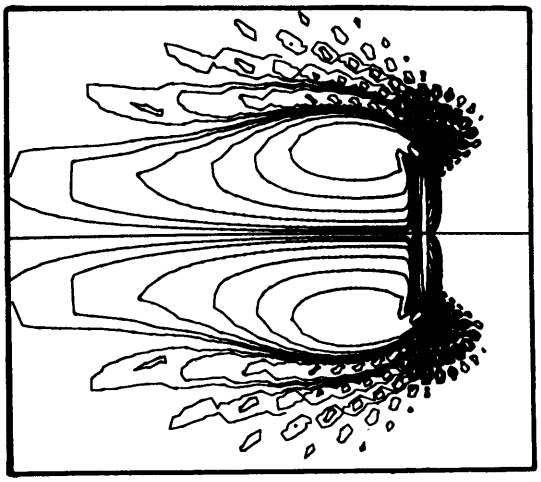

b. $C_{V\ min}$=0.0625

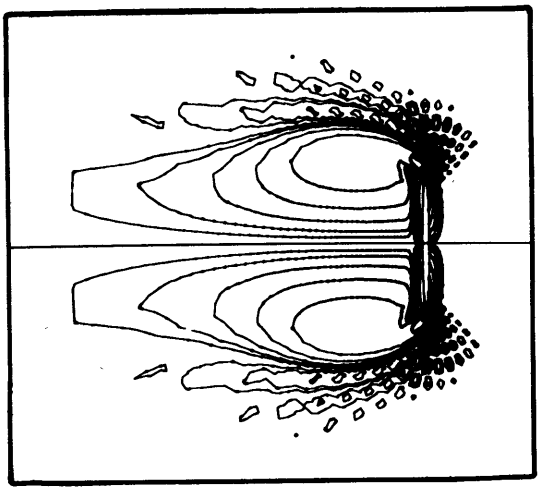

c. $C_{V\ min}$=0.125

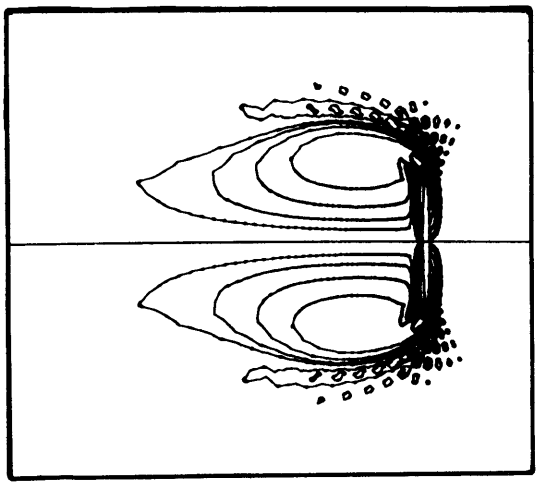

d. $C_{V\ min}$=0.25

Figure 9 – Equal-Vorticity Lines at R_e = 300 with Various Minimum Levels of Plotting $C_{V\,min}$

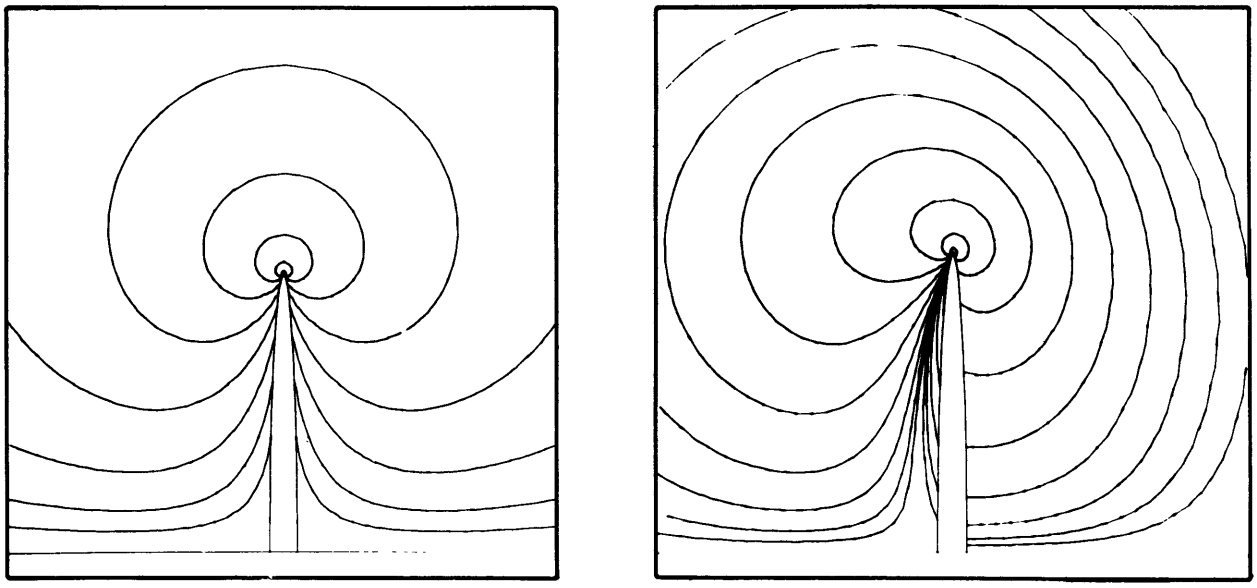

a. $R_e = 0$

b. $R_e = 10$

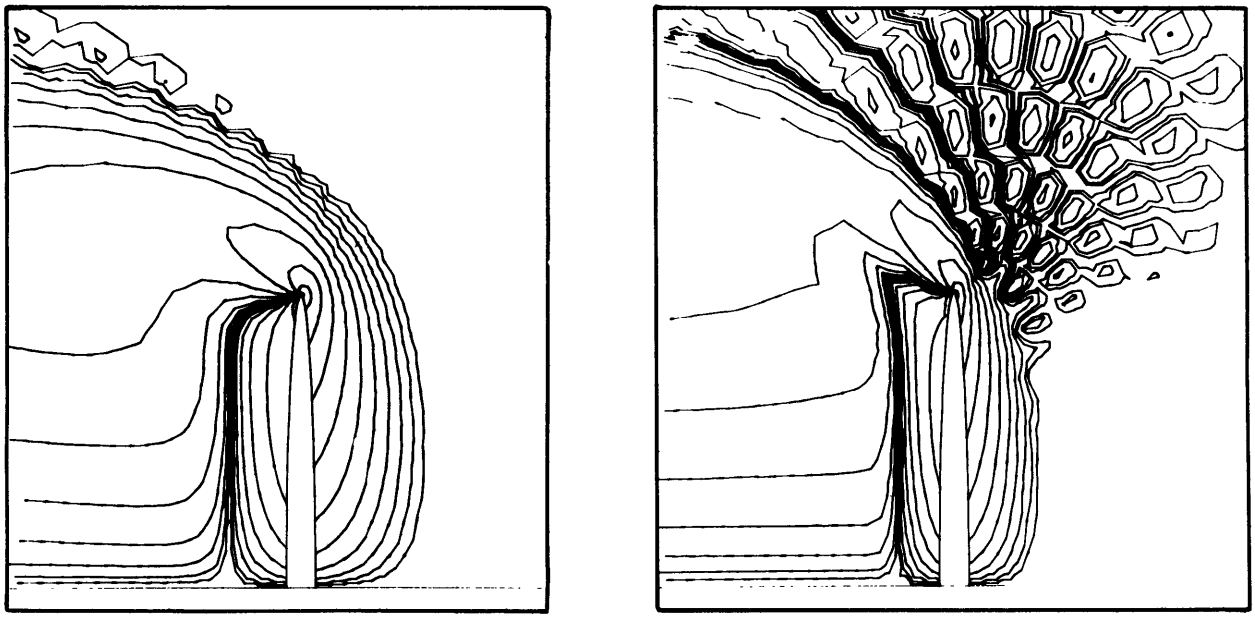

c. $R_e = 100$

d. $R_e = 300$

Figure 10 – Equal-Vorticity Lines in the Vicinity of the Disk for Various Reynolds Numbers

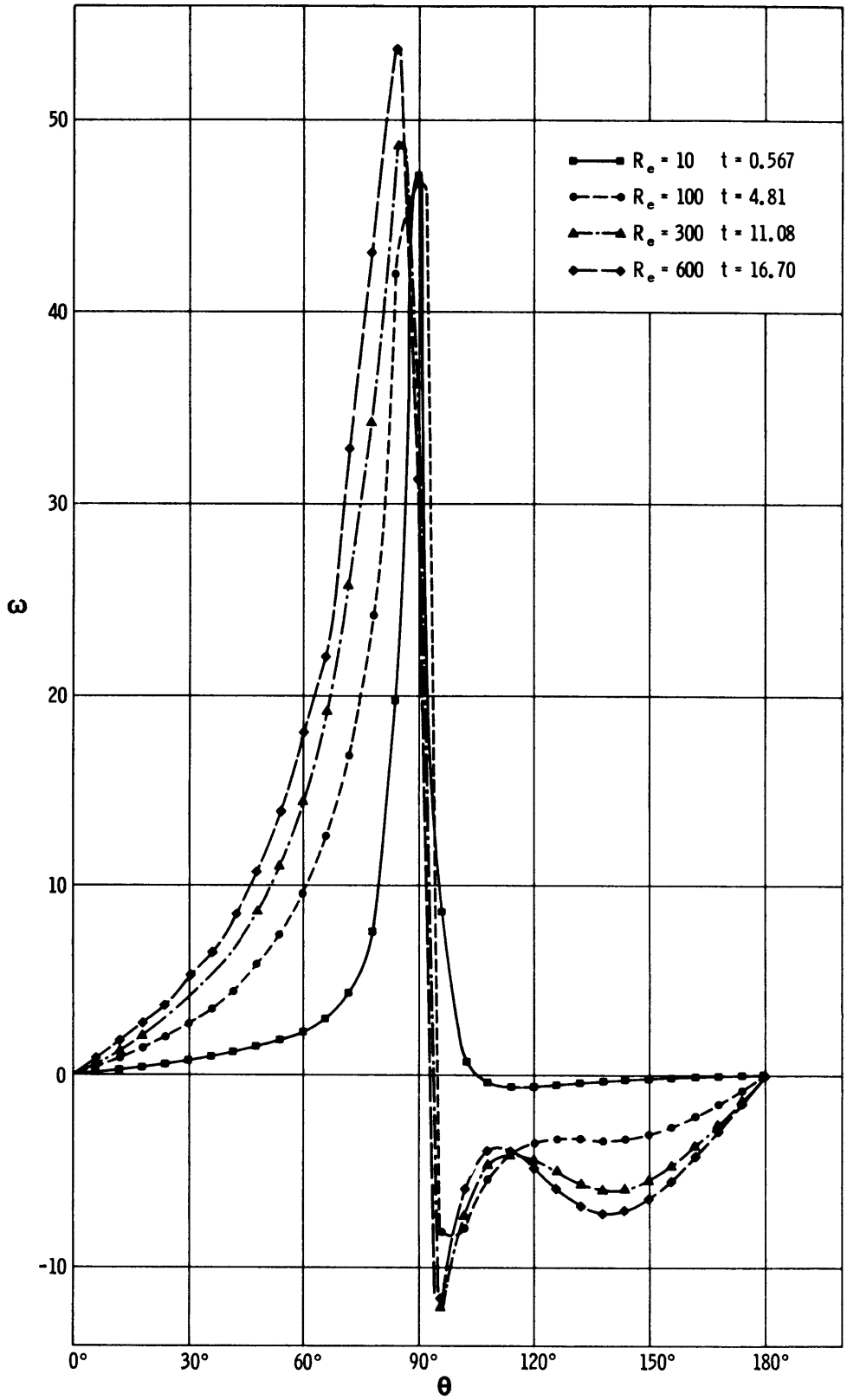

Figure 11 – Vorticity Distribution on a Disk of Thickness $\eta_b = 0.05$ for Various Reynolds Numbers

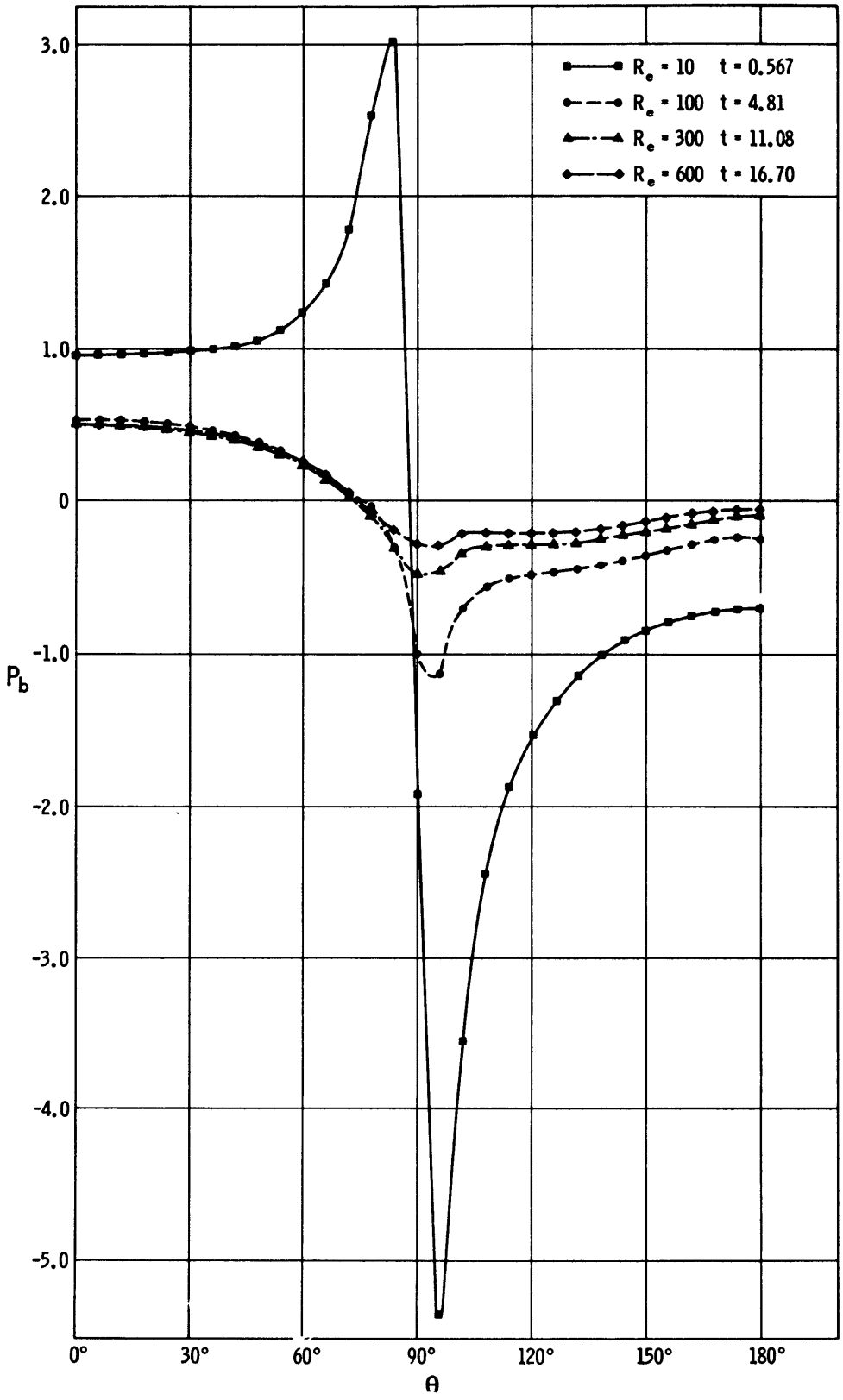

Figure 12 – Pressure Distribution on a Disk of Thickness $\eta_b = 0.05$ for Various Reynolds Numbers

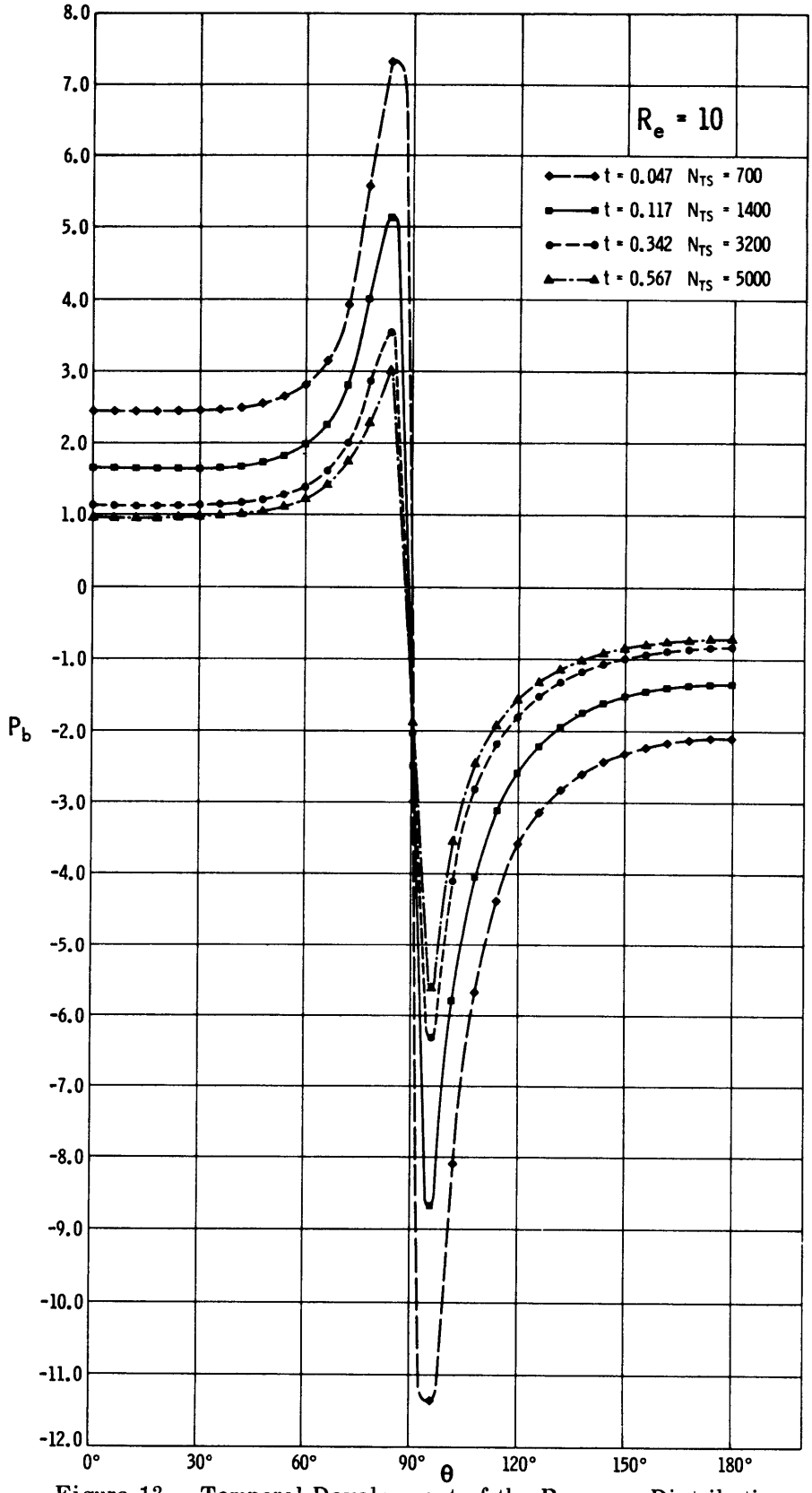

Figure 13 – Temporal Development of the Pressure Distribution on the Disk at $R_e = 10$

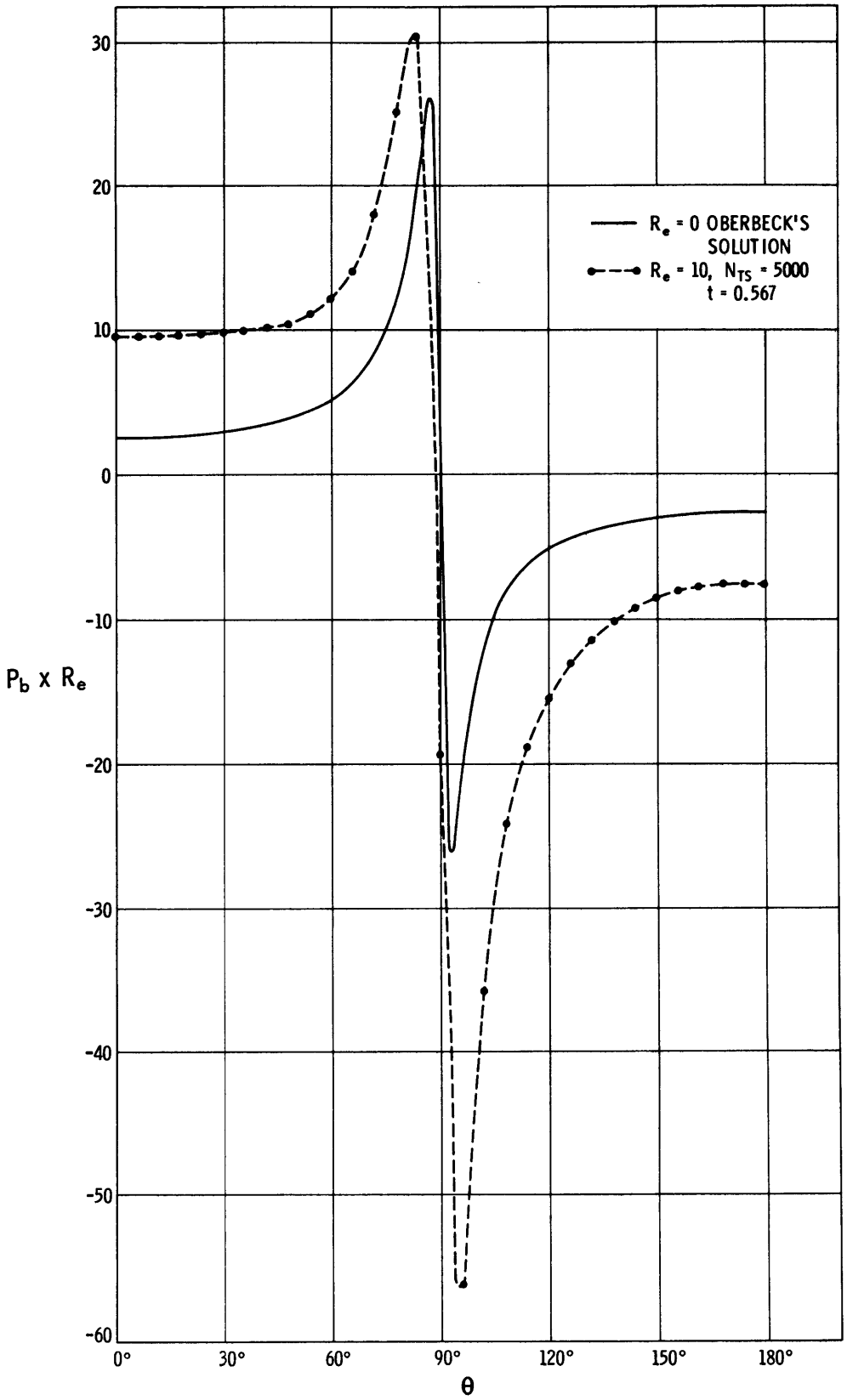

Figure 14 – $P_b \times R_e$ Distribution on the Disk at $R_e = 10$ and $R_e = 0$

Slow motion solution of Oberbeck.

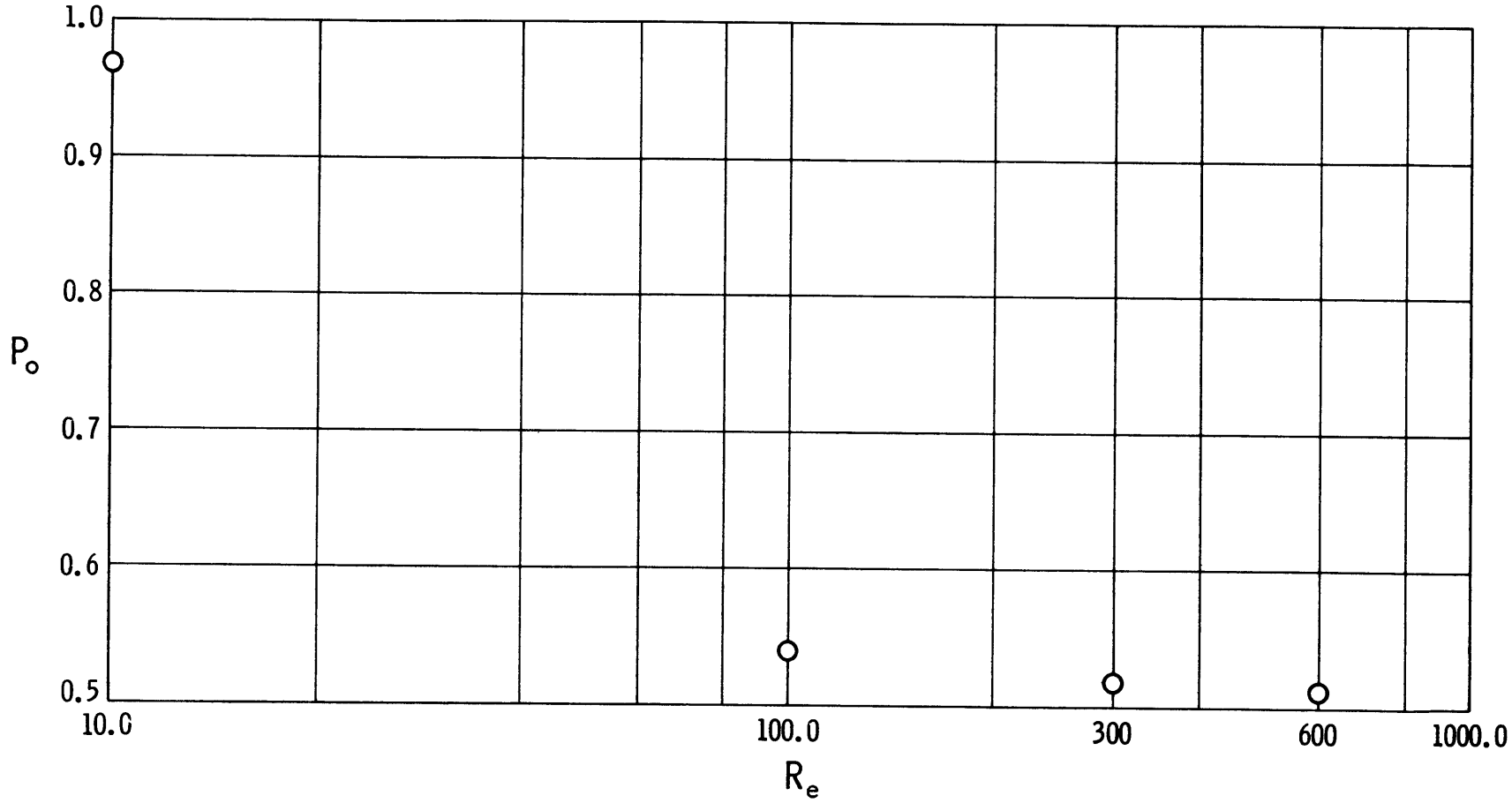

Figure 15 – Stagnation Pressure P_0 versus Reynolds Number R_e

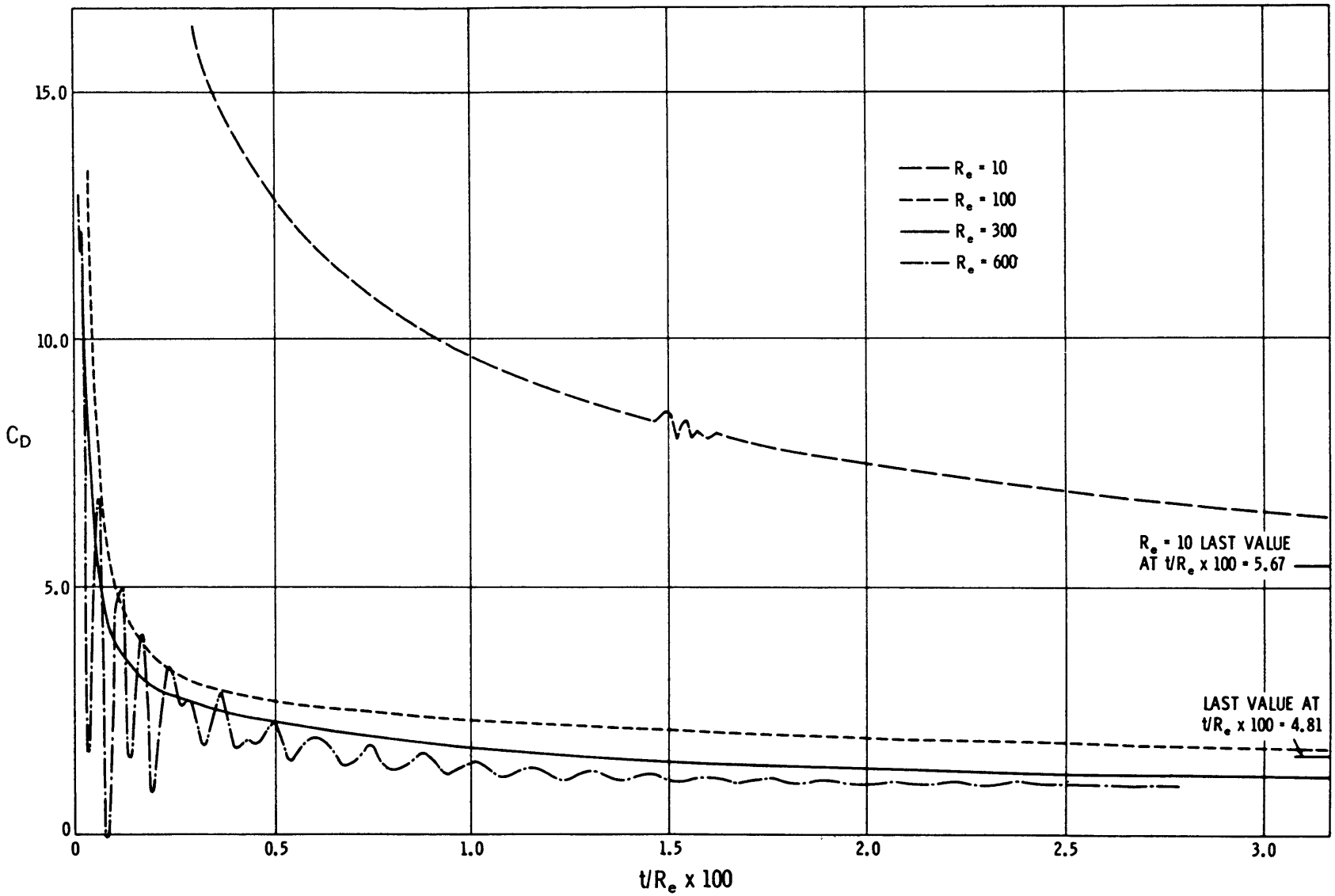

Figure 16 – Drag Coefficient C_D versus Time $t/R_e \times 100$

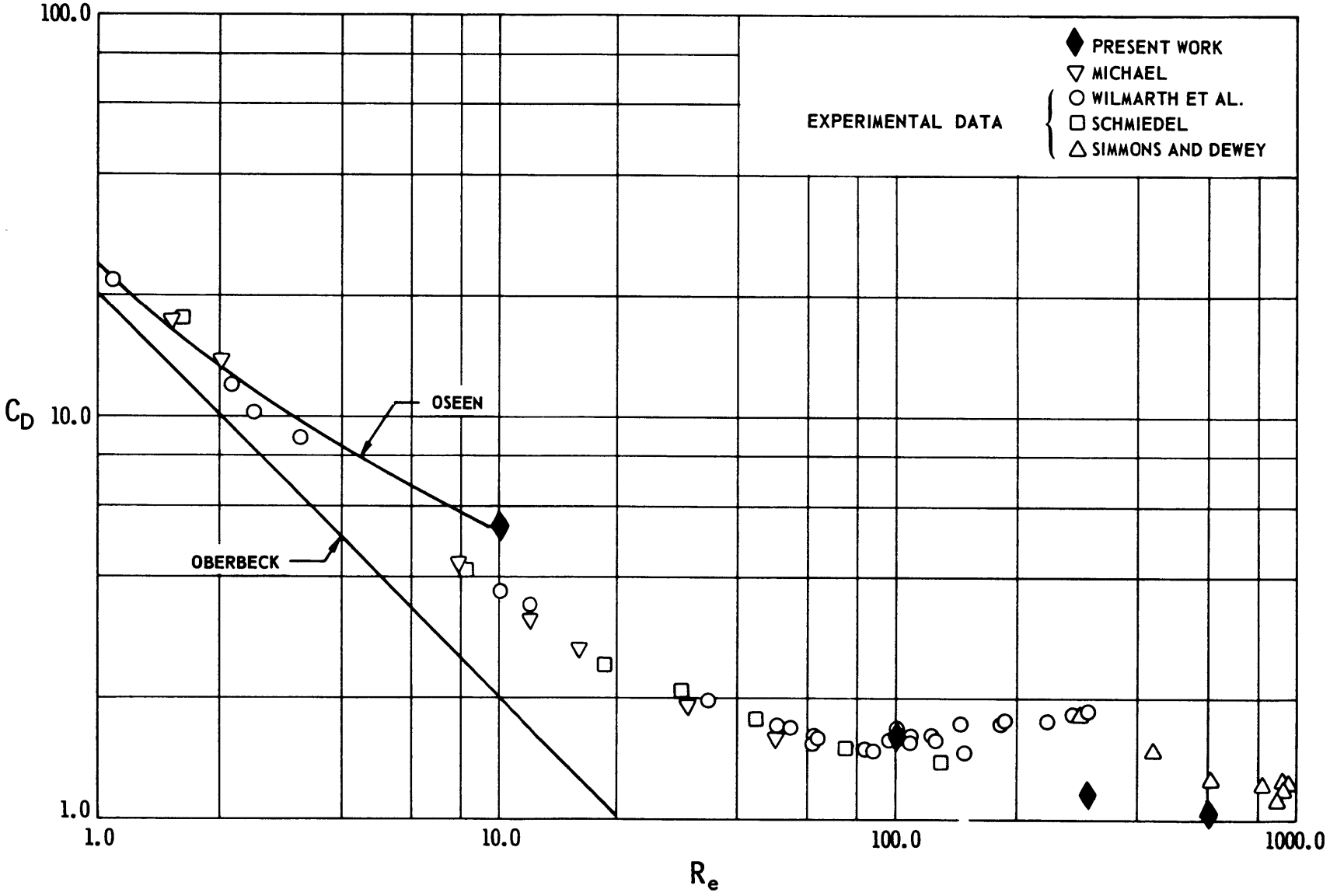

Figure 17 – Drag Coefficient C_D versus Reynolds Number R_e for a Disk in a Uniform Flow

TABLE 1

Terminal Values of Some Representative Quantities

Re	10	100	300	600
NTS	5000	4500	4000	3000
t_L	0.56715	4.81360	11.0822	16.7041
δt_L	0.000125	0.00125	0.00375	0.0072
C_{DP}	5.1717	1.5768	1.1508	1.0136
C_{DF}	0.2700	0.0330	0.0118	0.006653
C_D	5.4417	1.6098	1.1626	1.0203
P_0	0.96898	0.54016	0.51689	0.51101

REFERENCES

1. Wilmarth, W.W. et al., "Steady and Unsteady Motions and Wakes of Freely Falling Disks," The Physics of Fluids, Vol. 7, pp. 197–208 (1964).

2. Simmons, L.F.G. and Dewy, N.S., "Wind Tunnel Experiments with Circular Discs," Aero. Res. Com. (Gr. Brit.) Mem. Report 1334 (1930).

3. Schmiedel, J., "Experimentelle Untersuchungen uber die Fallbewegung von Kugeln and Scheiben in reibenden Flussigkeiten," Physik. Z., Vol. 29, pp. 593–610 (1928).

4. Lugt, H.J. and Schwiderski, E.W., "Flows around Dihedral Angles: I. Eigenmotion Analysis, II. Analysis of Regular and Singular Motions," Proc. of the Royal Soc., Ser. A, Vol. 285, pp. 382–412 (1965).

5. Carrier, G.F. and Lin, C.C., "On the Nature of the Boundary Layer near the Edge of a Flat Plate," Quart. Appl. Math., Vol. 6, pp. 63–68 (1948).

6. Thom, A., "An Investigation of Fluid Flow in Two Dimensions," Aero. Res. Com. (Gr. Brit.) Mem. Report 1194 (Nov 1928).

7. Fromm, J.E., "A Method for Computing Non-Steady Incompressible Viscous Fluid-Flows," University of California Los Alamos Report LA 2910 (Sep 1963).

8. Payne, R.B., "Unsteady Viscous Flow Past a Circular Cylinder," Aero. Res. Com. (Gr. Brit.) Mem. Report 19694 (Nov 1957).

9. Thoman, D.C. and Szewczyk, A.A., "Numerical Solutions of Time Dependent Two-Dimensional Flow of a Viscous Incompressible Fluid Over Stationary and Rotating Cylinders," University of Notre Dame Technical Report 66-14 (Jul 1966).

10. Rimon, Y., "Numerical Solutions of the Time-Dependent Incompressible Viscous Flow over a Disk or a Sphere," Ph.D. dissertation, Princeton University (Jun 1967).

11. Magarvey, R.H. and Bishop, R.L., "Transition Ranges for Three-Dimensional Wakes," Can. J. of Physics, Vol. 39, pp. 1418–1422 (1961).

12. Michael, P., "Steady Motion of a Disk in a Viscous Fluid," Physics of Fluids, Vol. 9, pp. 466–471 (1966).

13. Happel, J. and Brenner, H., "Low Reynolds Numbers Hydrodynamics," Prentice Hall, Inc. (1965).

14. Lamb, H., "Hydrodynamics," Dover Publications, Inc., New York, Sixth Edition, Chap. V., p. 107 (1945).

15. Homann, F., "The Effect of High Viscosity of the Flow around a Cylinder and a Sphere," NACA Tech. Mem. 1334 (Jun 1952).

INITIAL DISTRIBUTION

Copies

- 4 NAVSHIPSYSCOM
  - 1 SHIPS 031
  - 1 SHIPS 0311
  - 2 SHIPS 2052
- 1 DNL
- 7 CHONR
  - 1 Dr. P. King
  - 1 Dr. S. Silverman
  - 1 Mr. M. Cooper
  - 1 Mr. R.D. Cooper
  - 1 Dr. R.D. Ryan
  - 1 Dr. B.J. MacDonald
  - 1 Dr. L.D. Bram
- 1 NRL
  - 1 Tech Lib
- 1 NOL
  - 1 Tech Lib
- 1 NWC
  - 1 Tech Lib
- 5 NWL
  - 1 Dr. C.J. Cohen
  - 1 Dr. A.V. Hershey
  - 1 Dr. E.W. Schwiderski
  - 1 Dr. B. Zondek
  - 1 Tech Lib
- 1 NUWC
  - 1 Tech Lib
- 1 NELC
  - 1 Tech Lib
- 2 NRDL (Naval Radiological Def Lab)
  - 1 Dr. J.W. Pritchett
  - 1 Tech Lib
- 2 Naval PGSCOL, Monterey
  - 1 Dr. T.H. Gawain
  - 1 Tech Lib
- 2 USNA
  - 1 Dept of Mathe
  - 1 Tech Lib
- 20 DDC

Copies

- 2 US Army Math Res Center
  Univ of Wisconsin, Madison
  - 1 Dr. D. Greenspan
  - 1 Tech Lib
- 1 US Army Res Office
  Durham, N.C. 27706
  CRD-AA-IPL Box CM
- 1 NASA, Washington
  - 1 Tech Lib
- 1 NASA Marshal Space Flight Ctr
  Huntsville, Ala 35809
  - 1 Tech Lib
- 1 NASA Lewis Res Center
  Cleveland, Ohio 44121
  - 1 Tech Lib
- 2 NASA Ames Res Ctr
  Moffet Field, Calif 94305
  - 1 Dr. W.J. McCroskey
  - 1 Tech Lib
- 1 NASA Langley Field
  - 1 Tech Lib
- 1 USAEC
  - 1 Tech Lib
- 1 Oak Ridge National Lab
  - 1 Tech Lib
- 4 Los Alamos Sci Lab
  Los Alamos, New Mexico 87544
  - 1 Dr. F.H. Harlow
  - 1 Dr. C.W. Hirt
  - 1 Dr. B.J. Daly
  - 1 Tech Lib
- 3 Brookhaven National Lab
  Upton, Long Island, N.Y.
  - 1 Dr. P. Michael
  - 1 Dr. D.W. Lick
  - 1 Tech Lib
- 3 NBS
  - 1 Dr. H. Oser
  - 1 Dr. W. Sadowski
  - 1 Tech Lib

Copies

2 Natl Sci Foundation
1520 H St., N.W., Washington, D.C. 20550
1 Mathe Sci Div
1 Engin Sci Div

6 Princeton University
1 Prof S.I. Cheng
1 Dr. J. Smagorinski
1 Dr. L. Rintel
1 Dr. K. Bryan
1 Aerospace & Mech Eng Lib
1 Prof M. Kruskal

3 Harvard University
1 Prof S. Goldstein
1 Prof G. Birkhoff
1 Prof F.G. Carrier

5 MIT Cambridge, Mass
1 Prof C.C. Lin
1 Prof A.H. Shapiro
1 Prof H.P. Greenspan
1 Prof S.A. Orszag
1 Mr. M. Israeli, Appl Math Dept

2 Univ of Maryland
College Park, Maryland
1 Prof A.J. Faller
1 Prof A. Plotkin

1 Yale University
1 Dr. U. Navon

3 Courant Inst of Math Sci
N.Y.U., New York, N.Y.
1 Prof H.B. Keller
1 Dr. A.J. Chorin
1 Dr. Burstein

5 Stanford Univ
1 Prof A. Acrivos
1 Dr. L.G. Leal
1 Prof M.D. Van Dyke
1 Prof I. Flugge-Lotz
1 Mr. W.H. Frey, Eng Dept

2 Polytechnic Inst of Brooklyn
1 Prof G. Moretti
1 Prof R.C. Ackerberg

4 N.C.A.R., Boulder, Colorado 80301
1 Dr. D.K. Lilly
1 Dr. A. Kasahara
1 Dr. J.W. Deardorff
1 Dr. P. Kornfeld

Copies

2 Bell Tele Labs, Whippany, N.J. 07981
1 Dr. G.S. Deem
1 Dr. N.J. Zabusky

3 General Elec Space Sci Lab
Valley Forge, P.O. 8555
Philadelphia, Pa. 19101
1 Dr. S.M. Scala
1 Dr. P. Gordon
1 Dr. R. Shani

1 Prof K. Aziz
Univ of Kalgary, Kalgary 44
Alberta, Canada

1 Prof J.S. Allen
The Pennsylvania State Univ
Dept of Aerospace Eng
University Park, Pa. 16802

1 Prof S.C.R. Dennis
Dept of Applied Math
Univ of Western Ontario
London, Ontario, Canada

1 Dr. J.E. Fromm
Dept 977, Bldg 025
Res Div, IBM Corp
Monterey and Cottle Road
San Jose, Calif 95114

1 Dr. U. Shafrir
Space Sci & Eng Center
Univ of Wisconsin
Madison, Wisconsin 53706

1 Dr. C.W. van Atta
Univ of California
La Jolla, Calif 92037

1 Dr. E.R. van Driest
North American Rockwell Corp
350 South Magnolia Ave
Long Beach, Calif 90802

1 Prof A.E. Hamielec
McMaster Univ
Hamilton, Ontario, Canada

1 Prof S. Kaniel
Dept of Mathe
Northwestern Univ
Evanston, Illinois

Copies

1 Dr. P.J. Roache
Div 9325 Sandia Lab
Albuquerque, N. Mexico 87115

1 Dr. S.L. Slotta
Oregon State Univ
Corvalis, Oregon 97331

1 Prof W.W. Wilmarth
The Univ of Michigan
1077 East Engineering Bldg
Ann Arbor, Michigan 48104

1 Dr. H.C. Kao
Northrop Norair
Orgn No. 3713, Zone 31
3901 West Broadway
Hawthorne, Calif 90250

3 Boeing Sci Res Lab
P.O. 398, Seattle, Washington
1 Dr. A. Goldberg
1 Dr. Y.H. Pao
1 Dr. E.M. Murman

2 University of Notre Dame
1 Prof A.A. Szewczyk
1 Prof S.A. Piacsek

1 Dr. D. Thoman
C23 E. Mishawaha Ave
Mishawaha, Indiana

1 Mr. G.N. Slinn
Battelle Memorial Inst
P.O. 999
Richland, Washington 99352

1 Prof R. Manohar
Univ of Saskatchewan
Saskatoon, Canada

1 Prof Z. Lavan
Illinois Institute of Tech
Chicago, Illinois 60616

1 Mr. J.T. Obrien
US Naval Civil Engineering Lab
Port Hueneme, Calif 93041

Copies

1 Prof H.H. Chiu
Dept of Aero & Astro
University Heights, New York, N.Y. 10453

1 Prof K.E. Torrence
Cornell Univ
Ithaca, New York

UNCLASSIFIED

Security Classification

DOCUMENT CONTROL DATA - R & D

(Security classification of title, body of abstract and indexing annotation must be entered when the overall report is classified)

1. ORIGINATING ACTIVITY (Corporate author)	2a. REPORT SECURITY CLASSIFICATION
Naval Ship Research and Development Center Washington, D.C. 20007	UNCLASSIFIED
	2b. GROUP

3. REPORT TITLE

NUMERICAL SOLUTION OF THE INCOMPRESSIBLE TIME-DEPENDENT VISCOUS FLOW PAST A THIN OBLATE SPHEROID

4. DESCRIPTIVE NOTES (Type of report and inclusive dates)

Final Report

5. AUTHOR(S) (First name, middle initial, last name)

Yermiyahu Rimon

6. REPORT DATE	7a. TOTAL NO. OF PAGES	7b. NO. OF REFS
Jan 1969	52	15

8a. CONTRACT OR GRANT NO.	9a. ORIGINATOR'S REPORT NUMBER(S)
b. PROJECT NO. S-R003 10 01 Task 11572	2955
c.	9b. OTHER REPORT NO(S) (Any other numbers that may be assigned this report)
d.	

10. DISTRIBUTION STATEMENT

This report has been approved for public release and sale; its distribution is unlimited.

11. SUPPLEMENTARY NOTES	12. SPONSORING MILITARY ACTIVITY
	NAVSHIPS

13. ABSTRACT

The objective of this work is to obtain numerical solutions of the transient flow around a thin disk normal to the flow. The transition takes place between a potential field and a fully developed viscous field. The fluid is incompressible and homogeneous, and its flow is governed by the Navier-Stokes equations.

The purpose of the study is twofold: (1) to investigate the effects of a very large curvature of the body on the numerical procedure for the solution of the flow field and (2) to investigate the fundamental fluid dynamical phenomena of separation, of a recirculatory wake, and of vorticity shedding under the constraint of axial symmetry.

The solutions are obtained by constructing a finite-difference approximation to the Navier-Stokes equations on an oblate spheroidal grid system, and then advancing the solution with respect to time. The vorticity and the stream function are the dependent variables.

The results show that no vorticity shedding occurs for axisymmetric flow in the Reynolds-number range studied. In addition, some new interesting fluid-dynamical features are revealed. These include a different behavior of the pressure distribution at low and high Reynolds numbers and a local maximum of vorticity inside the wake at the higher Reynolds numbers studied.

14 KEY WORDS	LINK A		LINK B		LINK C	
	ROLE	WT	ROLE	WT	ROLE	WT
Navier-Stokes Equations						
Viscous Flow						
Numerical Solution						
Flow around a Disk						

Naval Ship Research and Development Center. Report 2955.
NUMERICAL SOLUTION OF THE INCOMPRESSIBLE TIME-DEPENDENT VISCOUS FLOW PAST A THIN OBLATE SPHEROID, by Yermiyahu Rimon. Jan 1969. v, 47p.
UNCLASSIFIED

The objective of this work is to obtain numerical solutions of the transient flow around a thin disk normal to the flow. The transition takes place between a potential field and a fully developed viscous field. The fluid is incompressible and homogeneous, and its flow is governed by the Navier-Stokes equations.

The purpose of the study is twofold: (1) to investigate the effects of a very large curvature of the body on the numerical procedure for the solution of the flow field and (2) to investigate the fundamental fluid dynamical phenomena of separation, of a recirculatory wake, and of vorticity shedding under the constraint of axial symmetry.

1. Oblate spheroids (Thin)--Flow field--Numerical solutions
2. Disks--Fluid flow--Numerical solutions
3. Viscous flow
4. Navier-Stokes equations
5. Numerical solutions
I. Rimon, Yermiyahu

Naval Ship Research and Development Center. Report 2955.
NUMERICAL SOLUTION OF THE INCOMPRESSIBLE TIME-DEPENDENT VISCOUS FLOW PAST A THIN OBLATE SPHEROID, by Yermiyahu Rimon. Jan 1969. v, 47p.
UNCLASSIFIED

The objective of this work is to obtain numerical solutions of the transient flow around a thin disk normal to the flow. The transition takes place between a potential field and a fully developed viscous field. The fluid is incompressible and homogeneous, and its flow is governed by the Navier-Stokes equations.

The purpose of the study is twofold: (1) to investigate the effects of a very large curvature of the body on the numerical procedure for the solution of the flow field and (2) to investigate the fundamental fluid dynamical phenomena of separation, of a recirculatory wake, and of vorticity shedding under the constraint of axial symmetry.

1. Oblate spheroids (Thin)--Flow field--Numerical solutions
2. Disks--Fluid flow--Numerical solutions
3. Viscous flow
4. Navier-Stokes equations
5. Numerical solutions
I. Rimon, Yermiyahu

Naval Ship Research and Development Center. Report 2955.
NUMERICAL SOLUTION OF THE INCOMPRESSIBLE TIME-DEPENDENT VISCOUS FLOW PAST A THIN OBLATE SPHEROID, by Yermiyahu Rimon. Jan 1969. v, 47p.
UNCLASSIFIED

The objective of this work is to obtain numerical solutions of the transient flow around a thin disk normal to the flow. The transition takes place between a potential field and a fully developed viscous field. The fluid is incompressible and homogeneous, and its flow is governed by the Navier-Stokes equations.

The purpose of the study is twofold: (1) to investigate the effects of a very large curvature of the body on the numerical procedure for the solution of the flow field and (2) to investigate the fundamental fluid dynamical phenomena of separation, of a recirculatory wake, and of vorticity shedding under the constraint of axial symmetry.

1. Oblate spheroids (Thin)--Flow field--Numerical solutions
2. Disks--Fluid flow--Numerical solutions
3. Viscous flow
4. Navier-Stokes equations
5. Numerical solutions
I. Rimon, Yermiyahu

Naval Ship Research and Development Center. Report 2955.
NUMERICAL SOLUTION OF THE INCOMPRESSIBLE TIME-DEPENDENT VISCOUS FLOW PAST A THIN OBLATE SPHEROID, by Yermiyahu Rimon. Jan 1969. v, 47p.
UNCLASSIFIED

The objective of this work is to obtain numerical solutions of the transient flow around a thin disk normal to the flow. The transition takes place between a potential field and a fully developed viscous field. The fluid is incompressible and homogeneous, and its flow is governed by the Navier-Stokes equations.

The purpose of the study is twofold: (1) to investigate the effects of a very large curvature of the body on the numerical procedure for the solution of the flow field and (2) to investigate the fundamental fluid dynamical phenomena of separation, of a recirculatory wake, and of vorticity shedding under the constraint of axial symmetry.

1. Oblate spheroids (Thin)--Flow field--Numerical solutions
2. Disks--Fluid flow--Numerical solutions
3. Viscous flow
4. Navier-Stokes equations
5. Numerical solutions
I. Rimon, Yermiyahu

The solutions are obtained by constructing a finite-difference approximation to the Navier-Stokes equations on an oblate spheroidal grid system, and then advancing the solution with respect to time. The vorticity and the stream function are the dependent variables.

The results show that no vorticity shedding occurs for axisymmetric flow in the Reynolds-number range studied. In addition, some new interesting fluid-dynamical features are revealed. These include a different behavior of the pressure distribution at low and high Reynolds numbers and a local maximum of vorticity inside the wake at the higher Reynolds numbers studied.

The solutions are obtained by constructing a finite-difference approximation to the Navier-Stokes equations on an oblate spheroidal grid system, and then advancing the solution with respect to time. The vorticity and the stream function are the dependent variables.

The results show that no vorticity shedding occurs for axisymmetric flow in the Reynolds-number range studied. In addition, some new interesting fluid-dynamical features are revealed. These include a different behavior of the pressure distribution at low and high Reynolds numbers and a local maximum of vorticity inside the wake at the higher Reynolds numbers studied.

The solutions are obtained by constructing a finite-difference approximation to the Navier-Stokes equations on an oblate spheroidal grid system, and then advancing the solution with respect to time. The vorticity and the stream function are the dependent variables.

The results show that no vorticity shedding occurs for axisymmetric flow in the Reynolds-number range studied. In addition, some new interesting fluid-dynamical features are revealed. These include a different behavior of the pressure distribution at low and high Reynolds numbers and a local maximum of vorticity inside the wake at the higher Reynolds numbers studied.

The solutions are obtained by constructing a finite-difference approximation to the Navier-Stokes equations on an oblate spheroidal grid system, and then advancing the solution with respect to time. The vorticity and the stream function are the dependent variables.

The results show that no vorticity shedding occurs for axisymmetric flow in the Reynolds-number range studied. In addition, some new interesting fluid-dynamical features are revealed. These include a different behavior of the pressure distribution at low and high Reynolds numbers and a local maximum of vorticity inside the wake at the higher Reynolds numbers studied.

Naval Ship Research and Development Center. Report 2955.
NUMERICAL SOLUTION OF THE INCOMPRESSIBLE TIME-DEPENDENT VISCOUS FLOW PAST A THIN OBLATE SPHEROID, by Yermiyahu Rimon. Jan 1969. v, 47p.
UNCLASSIFIED

The objective of this work is to obtain numerical solutions of the transient flow around a thin disk normal to the flow. The transition takes place between a potential field and a fully developed viscous field. The fluid is incompressible and homogeneous, and its flow is governed by the Navier-Stokes equations.

The purpose of the study is twofold: (1) to investigate the effects of a very large curvature of the body on the numerical procedure for the solution of the flow field and (2) to investigate the fundamental fluid dynamical phenomena of separation, of a recirculatory wake, and of vorticity shedding under the constraint of axial symmetry.

1. Oblate spheroids (Thin)--Flow field--Numerical solutions
2. Disks--Fluid flow--Numerical solutions
3. Viscous flow
4. Navier-Stokes equations
5. Numerical solutions
I. Rimon, Yermiyahu

Naval Ship Research and Development Center. Report 2955.
NUMERICAL SOLUTION OF THE INCOMPRESSIBLE TIME-DEPENDENT VISCOUS FLOW PAST A THIN OBLATE SPHEROID, by Yermiyahu Rimon. Jan 1969. v, 47p.
UNCLASSIFIED

The objective of this work is to obtain numerical solutions of the transient flow around a thin disk normal to the flow. The transition takes place between a potential field and a fully developed viscous field. The fluid is incompressible and homogeneous, and its flow is governed by the Navier-Stokes equations.

The purpose of the study is twofold: (1) to investigate the effects of a very large curvature of the body on the numerical procedure for the solution of the flow field and (2) to investigate the fundamental fluid dynamical phenomena of separation, of a recirculatory wake, and of vorticity shedding under the constraint of axial symmetry.

1. Oblate spheroids (Thin)--Flow field--Numerical solutions
2. Disks--Fluid flow--Numerical solutions
3. Viscous flow
4. Navier-Stokes equations
5. Numerical solutions
I. Rimon, Yermiyahu

Naval Ship Research and Development Center. Report 2955.
NUMERICAL SOLUTION OF THE INCOMPRESSIBLE TIME-DEPENDENT VISCOUS FLOW PAST A THIN OBLATE SPHEROID, by Yermiyahu Rimon. Jan 1969. v, 47p.
UNCLASSIFIED

The objective of this work is to obtain numerical solutions of the transient flow around a thin disk normal to the flow. The transition takes place between a potential field and a fully developed viscous field. The fluid is incompressible and homogeneous, and its flow is governed by the Navier-Stokes equations.

The purpose of the study is twofold: (1) to investigate the effects of a very large curvature of the body on the numerical procedure for the solution of the flow field and (2) to investigate the fundamental fluid dynamical phenomena of separation, of a recirculatory wake, and of vorticity shedding under the constraint of axial symmetry.

1. Oblate spheroids (Thin)--Flow field--Numerical solutions
2. Disks--Fluid flow--Numerical solutions
3. Viscous flow
4. Navier-Stokes equations
5. Numerical solutions
I. Rimon, Yermiyahu

Naval Ship Research and Development Center. Report 2955.
NUMERICAL SOLUTION OF THE INCOMPRESSIBLE TIME-DEPENDENT VISCOUS FLOW PAST A THIN OBLATE SPHEROID, by Yermiyahu Rimon. Jan 1969. v, 47p.
UNCLASSIFIED

The objective of this work is to obtain numerical solutions of the transient flow around a thin disk normal to the flow. The transition takes place between a potential field and a fully developed viscous field. The fluid is incompressible and homogeneous, and its flow is governed by the Navier-Stokes equations.

The purpose of the study is twofold: (1) to investigate the effects of a very large curvature of the body on the numerical procedure for the solution of the flow field and (2) to investigate the fundamental fluid dynamical phenomena of separation, of a recirculatory wake, and of vorticity shedding under the constraint of axial symmetry.

1. Oblate spheroids (Thin)--Flow field--Numerical solutions
2. Disks--Fluid flow--Numerical solutions
3. Viscous flow
4. Navier-Stokes equations
5. Numerical solutions
I. Rimon, Yermiyahu

The solutions are obtained by constructing a finite-difference approximation to the Navier-Stokes equations on an oblate spheroidal grid system, and then advancing the solution with respect to time. The vorticity and the stream function are the dependent variables.

The results show that no vorticity shedding occurs for axisymmetric flow in the Reynolds-number range studied. In addition, some new interesting fluid-dynamical features are revealed. These include a different behavior of the pressure distribution at low and high Reynolds numbers and a local maximum of vorticity inside the wake at the higher Reynolds numbers studied.

The solutions are obtained by constructing a finite-difference approximation to the Navier-Stokes equations on an oblate spheroidal grid system, and then advancing the solution with respect to time. The vorticity and the stream function are the dependent variables.

The results show that no vorticity shedding occurs for axisymmetric flow in the Reynolds-number range studied. In addition, some new interesting fluid-dynamical features are revealed. These include a different behavior of the pressure distribution at low and high Reynolds numbers and a local maximum of vorticity inside the wake at the higher Reynolds numbers studied.

The solutions are obtained by constructing a finite-difference approximation to the Navier-Stokes equations on an oblate spheroidal grid system, and then advancing the solution with respect to time. The vorticity and the stream function are the dependent variables.

The results show that no vorticity shedding occurs for axisymmetric flow in the Reynolds-number range studied. In addition, some new interesting fluid-dynamical features are revealed. These include a different behavior of the pressure distribution at low and high Reynolds numbers and a local maximum of vorticity inside the wake at the higher Reynolds numbers studied.

The solutions are obtained by constructing a finite-difference approximation to the Navier-Stokes equations on an oblate spheroidal grid system, and then advancing the solution with respect to time. The vorticity and the stream function are the dependent variables.

The results show that no vorticity shedding occurs for axisymmetric flow in the Reynolds-number range studied. In addition, some new interesting fluid-dynamical features are revealed. These include a different behavior of the pressure distribution at low and high Reynolds numbers and a local maximum of vorticity inside the wake at the higher Reynolds numbers studied.